# Data assimilative hindcast of the Gulf of Maine coastal circulation

Ruoying He,[1] Dennis J. McGillicuddy,[1] Daniel R. Lynch,[2] Keston W. Smith,[2] Charles A. Stock,[1] and James P. Manning[3]

[1] A data assimilative model hindcast of the Gulf of Maine (GOM) coastal circulation during an 11 day field survey in early summer 2003 is presented. In situ observations include surface winds, coastal sea levels, and shelf hydrography as well as moored and shipboard acoustic Doppler D current profiler (ADCP) currents. The hindcast system consists of both forward and inverse models. The forward model is a three-dimensional, nonlinear finite element ocean circulation model, and the inverse models are its linearized frequency domain and time domain counterparts. The model hindcast assimilates both coastal sea levels and ADCP current measurements via the inversion for the unknown sea level open boundary conditions. Model skill is evaluated by the divergence of the observed and modeled drifter trajectories. A mean drifter divergence rate $(1.78 \text{ km d}^{-1})$ is found, demonstrating the utility of the inverse data assimilation modeling system in the coastal ocean setting. Model hindcast also reveals complicated hydrodynamic structures and synoptic variability in the GOM coastal circulation and their influences on coastal water material property transport. The complex bottom bathymetric setting offshore of Penobscot and Casco bays is shown to be able to generate local upwelling and downwelling that may be important in local plankton dynamics.

**Citation:** He, R., D. J. McGillicuddy, D. R. Lynch, K. W. Smith, C. A. Stock, and J. P. Manning (2005), Data assimilative hindcast of the Gulf of Maine coastal circulation, *J. Geophys. Res.*, *110*, C10011, doi:10.1029/2004JC002807.

## 1. Introduction

[2] The Gulf of Maine (GOM) coastal circulation, consisting of a strong southwestward Maine Coastal Current (MCC) and several subbasin-scale gyres is primarily cyclonic [*Bigelow*, 1927; *Brooks*, 1985; *Brown and Irish*, 1992]. The circulation is driven by surface momentum and buoyancy fluxes as well as the pressure gradients set up by buoyancy of freshwater entering from the Scotian shelf and rivers along the Gulf coast relative to deep, salty continental slope water that enters through the Northeast Channel and fills the Gulf basins. Most of the general southwestward along-isobath flows in the Gulf exit through the Great South Channel and Nantucket shoals [*Beardsley et al.*, 1985]. The remainder is exchanged across the shelf-slope front on the south flank of Georges Bank [*Garfield and Evans*, 1987]. During the stratified season, the schematic view of the general circulation of the GOM is shown in Figure 1. Among many interesting coastal ocean dynamics and processes in this area, the MCC has been one of long-standing research topics [e.g., *Townsend et al.*, 1987; *Townsend*, 1991; *Franks*

*and Anderson*, 1992; *Lynch et al.*, 1997; *Pettigrew et al.*, 1998; *Geyer et al.*, 2004] because its structure and transport pathway have significant socioeconomic effects through nutrient and fish/lobster larvae transport and primary productivity including harmful algal blooms.

[3] The approaches taken by previous studies on the MCC have been based on either pure in situ observations or pure numerical model integrations where in situ measurements are used only to evaluate ocean model skill and performance. Although each approach has yielded tremendous knowledge about the GOM coastal circulation, in situ measurements alone often suffer under-sampling problems, whereas dynamic models alone often contain errors owing to misrepresentation of boundary conditions or other dynamic processes. Recent advancements in data assimilation techniques [e.g., *Mellor and Ezer*, 1991; *Bennett*, 1992; *Ezer and Mellor*, 1994; *Bowen et al.*, 1995; *Bogden et al.*, 1996; *Griffin and Thompson*, 1996; *Thompson and Griffin*, 1998; *Lewis et al.*, 1998; *Oke et al.*, 2002], by allowing in situ observations to constrain dynamic models, therefore promise improved understanding and modeling of coastal circulation.

[4] During the last several years, the Dartmouth modeling team has made significant progress in development of inverse techniques for ocean model data assimilation [*Lynch et al.*, 1998; *Lynch and Hannah*, 2001; *Lynch and Naimie*, 2002]. In those works the unknown sea level open boundary conditions are deduced from interior data subject to strong model constraints. By assimilating shipboard Acoustic

---

[1]Woods Hole Oceanographic Institution, Woods Hole, Massachusetts, USA.

[2]Thayer School of Engineering, Dartmouth College, Hanover, New Hampshire, USA.

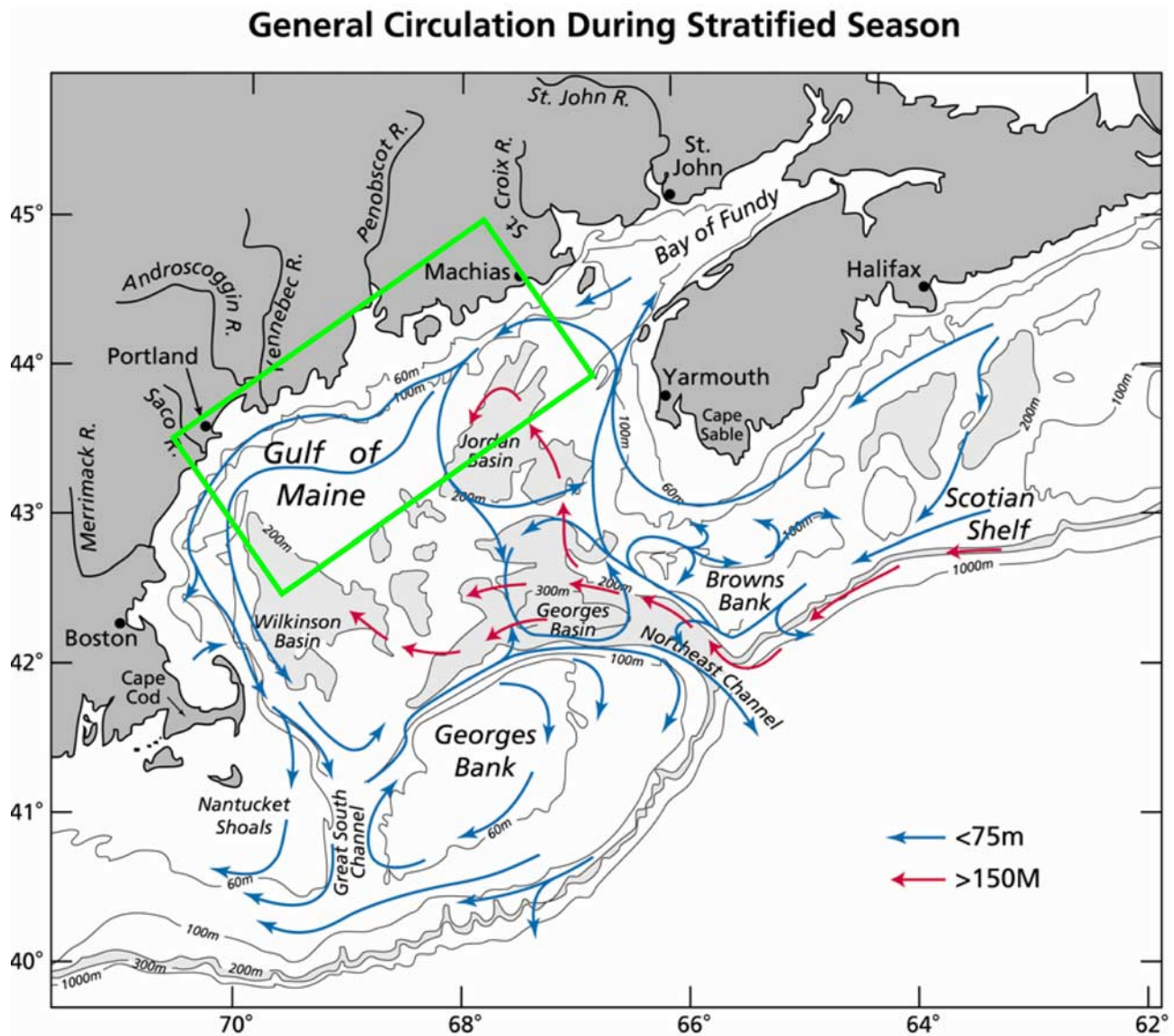[3]Northeast Fisheries Science Center, NOAA, Woods Hole, Massachusetts, USA.

**Figure 1.** General circulation of the Gulf of Maine in the stratified season [after *Beardsley et al.*, 1997]. The green box indicates the area of the field survey.

Doppler Current Profiler (ADCP) currents, the suite of forward and inverse models has been used successfully for both short-term real-time circulation nowcast/forecast [*Lynch et al.*, 2001] and circulation hindcasts [*Lynch and Hannah*, 2001; *Manning et al.*, 2001; *Lynch and Naimie*, 2002; *Proehl et al.*, 2005; *Aretxabaleta et al.*, 2005] on Georges Bank.

[5] In contrast to Georges Bank, the GOM coastal region is characterized by much more complex coastline (land boundary), bathymetric configurations (Figure 1), and highly variable surface forcing (owing to ocean-land interactions). In addition to the local forcing, the offshore fluxes across the active seaward boundary are also important in driving the GOM coastal circulation. For example, *Signell et al.* [1994] demonstrated the need for proper specification of the pressure field variability along the seaward open boundary to capture the observed tidal and subtidal flow patterns in Massachusetts

Bay. At larger scales, it is clear that the GOM coastal circulation features are intimately linked to gulf-wide circulation dynamics, with midgulf dynamics on seasonal [*Lynch et al.*, 1997] and wind band [*Holboke and Lynch*, 1995; *Holboke*, 1998; *Fan et al.*, 2005] timescales driving significant portions of well-known inshore features. At monthly timescales, pressure variations of order 5 cm were computed [*Lynch et al.*, 1997] along the cross-gulf boundary. GOM modeling approaches [e.g., *Lynch et al.*, 1996; *Signell et al.*, 1994; *Xue et al.*, 2000] to date have emphasized on either gulf-wide simulations, or various forms of nesting. The GOM coastal circulation therefore acts as an excellent test ground to examine the utility of Dartmouth inverse data assimilation technique in a general regional ocean setting.

[6] The objective of this study is to make use of in situ measurements collected by a GOM field survey in early
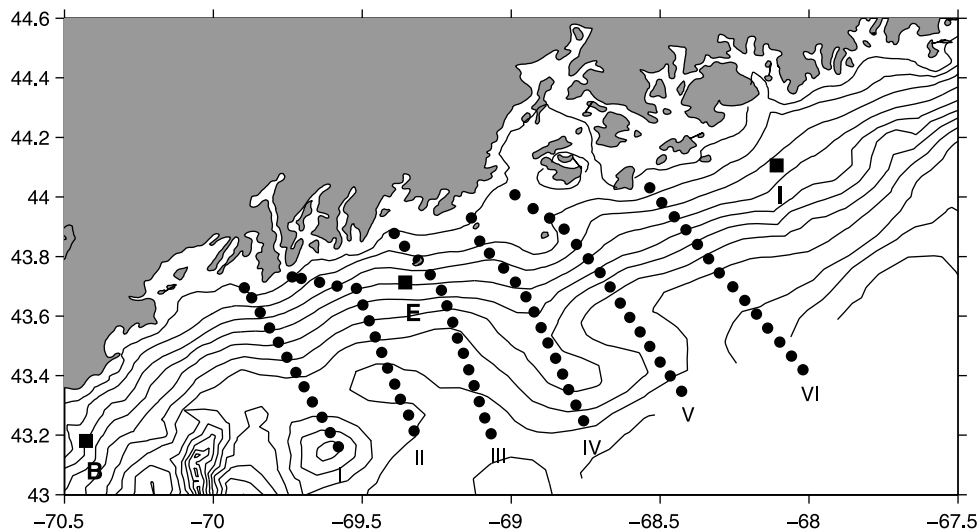
**Figure 2.** CTD stations of the survey (28 May to 7 June 2003). Survey along these six across-shelf transects (I-VI) were repeated three times back and forth with a total of 256 CTD casts made during 11 days at sea. GOMOOS ADCP moorings B, E, and I are denoted by the squares.

summer 2003 to perform inverse data assimilative model hindcast of the coastal circulation, to assess the skill of the data assimilative model, and to infer important physical processes responsible for coastal water property transport. Moreover, only ADCP currents were assimilated in the aforementioned Georges Bank circulation studies. Since coastal tide gauge sea level observations are the most complete and easily accessible in situ observations in the coastal region, it is also our goal in this study to include coastal sea level data assimilation in the model hindcast, and draw inference as to the impacts of assimilating various data streams on coastal circulation prediction.

[7] The remainder of this paper is organized as follows. Section 2 reviews in situ measurements showing coastal oceanic and atmospheric conditions during the period of study. The Dartmouth inverse data assimilation system and the data inversion of open boundary sea levels are presented in section 3. Model hindcasts and in situ observations are compared in section 4. Section 5 presents detailed examinations of the model solutions at the subtidal timescale. This is followed by a set of DA sensitivity experiments on various data streams in section 6. Finally, section 7 summarizes and concludes the preceding material.

## 2. In Situ Observations

[8] In situ observations including shelf hydrography, shipboard ADCP currents, and biochemical variables were collected during a GOM field survey from 28 May to 7 June 2003. One of the scientific goals of this survey is to better understand and model the coastal hydrodynamics that can be used to infer the harmful algal bloom transport in the western GOM. The field survey focused on the coastal water between the Penobscot and Casco bays (as denoted by the green box in Figure 1), where harmful algal (*A. fundyense*) cells are often found in early summer of each year. CTD casts were made every 5 nautical miles along

6 across-shelf transects (Figure 2); The ship surveys were repeated three times back and forth in this area with a total of 256 CTD casts made during 11 days at sea.

[9] Shipboard ADCP simultaneously measured the underway currents throughout the water column. Without detiding, the currents inside the survey area (Figure 3) contain both tidal and subtidal variability, with current magnitude as large as 0.5 m s$^{-1}$. Aside strong tidal currents, the southwestward moving MCC is clearly discernable. This prominent coastal current is primarily the result of strong tidal rectification and basin-scale barotropic and baroclinic pressure gradients [*Lynch et al.*, 1997]. In addition to ship board ADCP current measurement, currents from three fixed moorings (B, E and I) of the Gulf of Maine Ocean Observing System (GOMOOS, http://www.gomoos.org/) were also collected. Buoy B is located on the western Maine shelf to the northwest of the Wilkinson Basin, whereas buoys E and I are located offshore of Casco Bay and Penobscot Bay, respectively. These fixed mooring current measurements, along with shipboard ADCP current measurements form the velocity data stream to be used in the inverse data assimilation.

[10] Coastal ocean circulation is often manifested by the sea level variability recorded by coastal tide gauges of National Ocean Service (NOS). For example, at both Boston and Portland stations, coastal sea levels (Figure 4) are evidently dominated by strong tidal components with amplitude of about 2 m. The low-pass-filtered renditions (scaled by the y axis on the right) of them have smaller magnitude (about 0.2 m), showing that during the time window of the field survey, the subtidal sea level rose between 31 May and 2 June, subsided between 3 and 4 June and rose again between 5 and 6 June. These variations were associated with strong downwelling favorable winds in the beginning of June and the subsequent upwelling and downwelling favorable wind conditions at later dates. Coastal sea level time series (not shown) at three other tide gauges (Bar Harbor, Cutler, and Eastport) along the coast
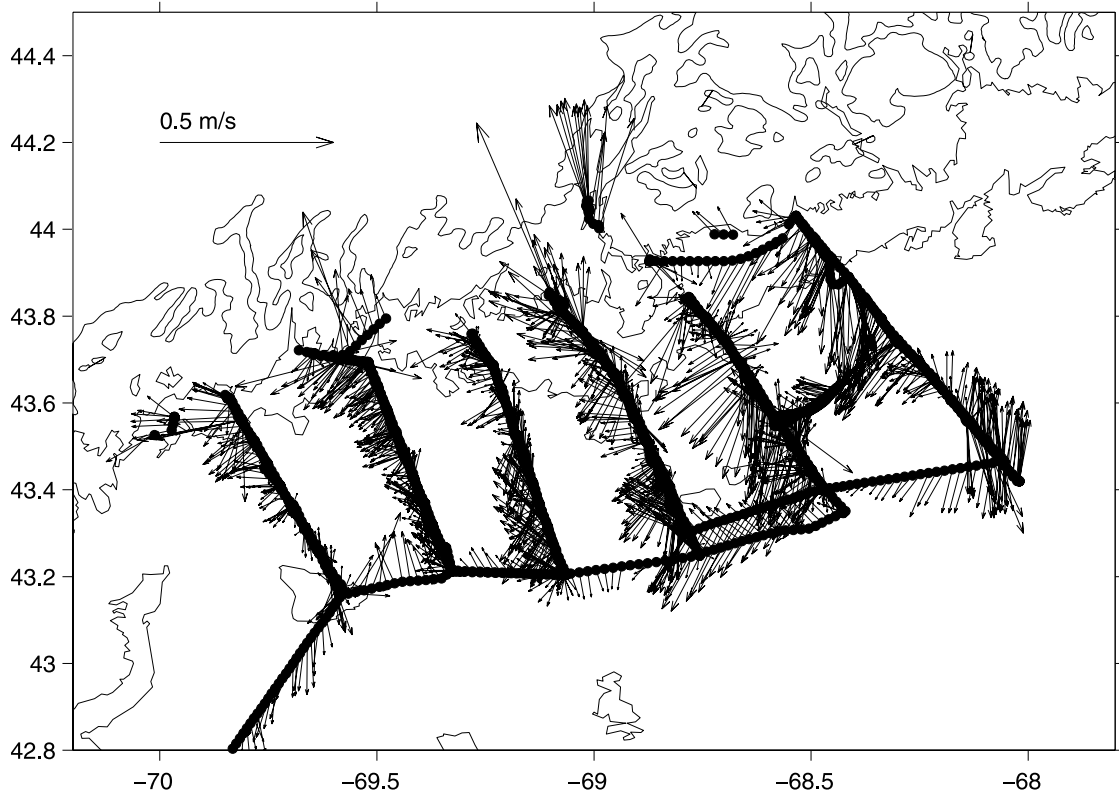
**Figure 3.** Depth-averaged shipboard ADCP current vectors measured in the field survey.
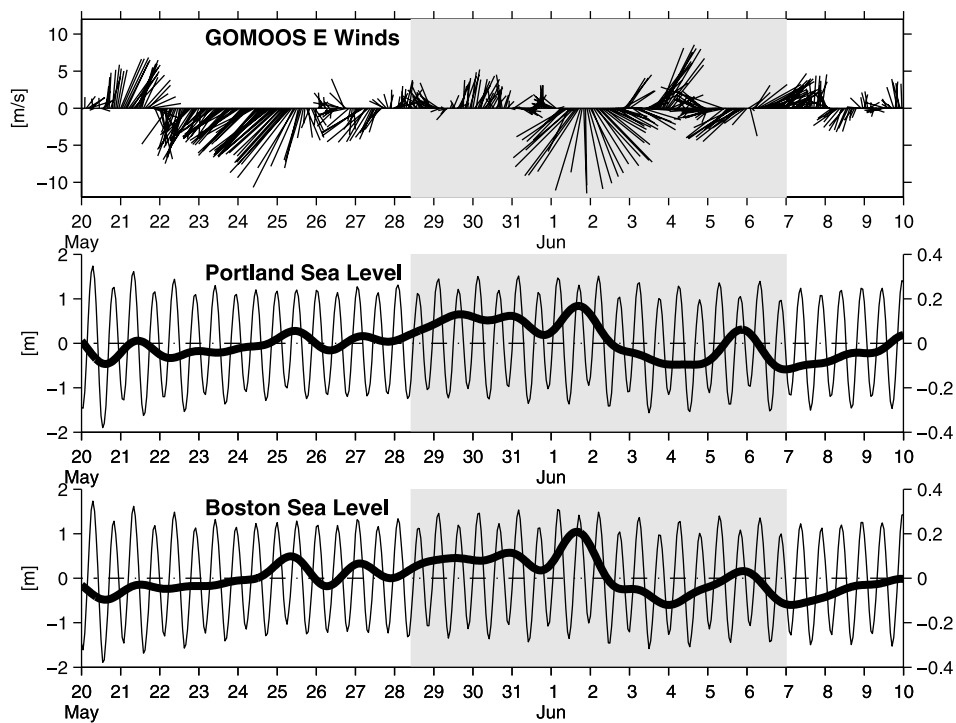


**Figure 4.** Time series of 36 hour low-pass-filtered wind vector (measured at GOMOOS mooring E) and coastal sea levels at Boston and Portland. The shaded area in each panel corresponds to the time window of field survey. Hourly and 36 hour low-pass-filtered sea levels are denoted by thin and thick lines, respectively.
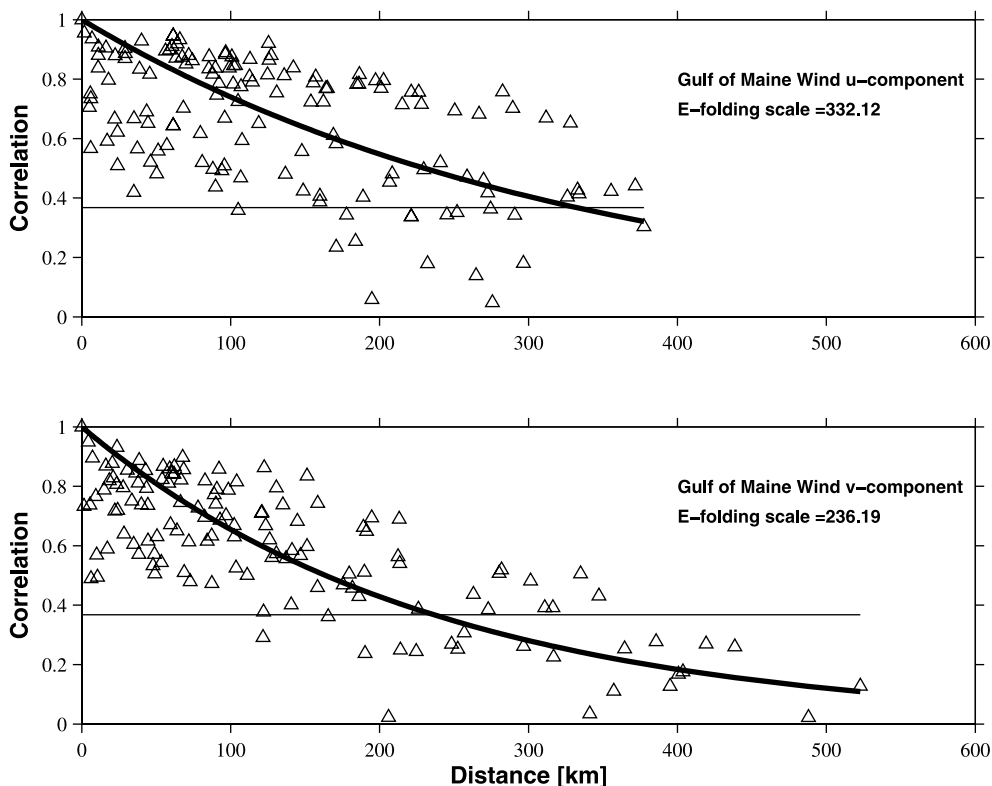
**Figure 5.** Autocorrelations of u (east-west) and v (north-south) components of wind observations (triangles). In each panel the exponential functional fitting (thick lines) indicate the spatial correlation scales are 332 (236 km) for wind u (v) components.

are also collected. Together, they comprise the sea level data stream to be used in the data assimilation experiments.

[11] Examinations of gulf-wide in situ wind measurements indicate clear spatial variability in gulf-wide surface wind fields. Such heterogeneity of the wind field is the result of complex air-sea and land-sea interactions in the coastal region, suggesting a single wind vector time series would not be sufficient to account for the gulf-wide wind variability that is pertinent to the coastal ocean response. Spatially varying wind fields usually are available from numerical weather predication model analyses. However, a more direct approach is to make use of all in situ wind measurements to reconstruct the wind fields through the optimal interpolation method [e.g., *He et al.*, 2004]. The spatial correlation scales of wind fields can be readily found by calculating the autocorrelations of $u$, and $v$ components of wind observations (Figure 5). Simple exponential functional fittings reveal that the spatial correlation scales for $u$ and $v$ components are 332 km and 236 km, respectively. These are in good agreement with previous study of *Fang and Brown* [1996]. With longer time series, they found the spatial correlation scale of the Gulf of Maine surface wind is ~300 km. Subsequent use of *Feng and Brown* [1996] wind fields was in model simulations of *Holboke and Lynch* [1995], and *Holboke* [1998]. Herein, the spatial varying wind field analyses between 20 May and 10 June are reconstructed with the optimal interpolation (OI) at 6-hourly time interval. Interested readers are referred to an animation of the complete OI wind fields online (http://ruoyingh. whoi.edu/MERHAB03/Paper). These OI wind fields are

used as the surface momentum forcing for the data assimilative model simulations to be discussed in section 3.

## 3. Model

[12] The Dartmouth data inverse model system consists of both forward and inverse modeling components. The data assimilation procedure is following: (1) the forward nonlinear model integration provides initial (prior) estimates of state variables, (2) the inverse models reduce the misfit between the data and the prior through adjustment of sea level open boundary conditions, (3) the forward simulation is then recomputed to produce the improved posterior solutions of the state variables. The misfit here is defined as the difference between the observations (vertically averaged ADCP currents and/or coastal sea levels) and the forward model solutions at data locations. This procedure is iterated, with the forward nonlinear model feeding friction, viscosity and misfit to the inverse models, to reduce a specified cost function. The open boundary control in the assimilation is the barotropic pressure. In these simulations it is the principal unmeasured but necessary boundary condition (baroclinic forcing is applied via buoyancy and wind stress). Accordingly, this control is determined in general by the barotropic misfit. Specifically, the ADCP misfit is averaged over the vertical sampling interval to filter out baroclinic component of the misfit, consistent with the dynamic hypothesis. Note that the depth-averaging procedure also help to avoid a potential sampling bias associated with more depth bins in deeper waters. Clearly, other
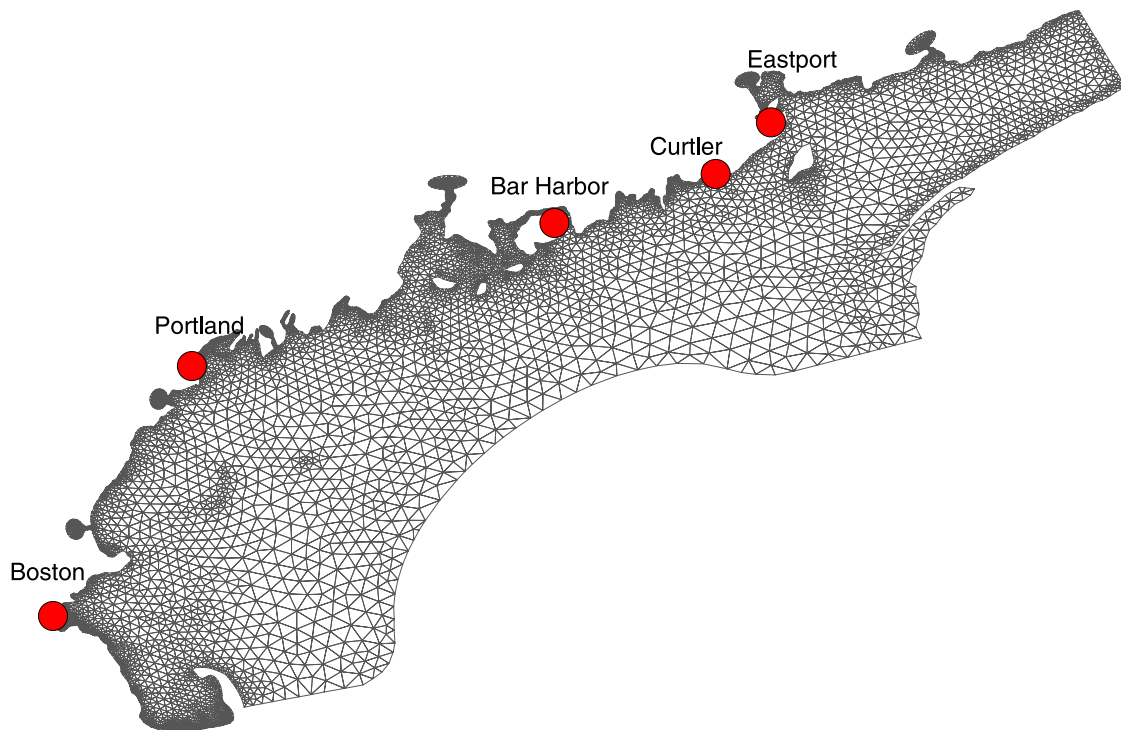
**Figure 6.** The unstructured mesh used in the data assimilative model hindcast. Coastal tidal gauges are indicated by dots.

treatments of ADCP currents are possible in different dynamical regimes. For example, *Proehl et al.* [2005] suggest more emphasis on the near-surface ADCP current could be appropriate for that particular application in the upper ocean.

[13] The forward ocean model used here is a finite element circulation model Quoddy, described in detail by *Lynch et al.* [1996]. The model is three-dimensional, hydrostatic, free surface, and fully nonlinear, with both barotropic and baroclinic motions resolved in tidal time-scales. Vertical mixing is represented by Mellor-Yamada 2.5 turbulence closure scheme [*Mellor and Yamada*, 1982; *Galperin et al.*, 1998]. Horizontal viscosity is represented by a mesh- and shear-dependent *Smagorinsky* [1963] scheme. A general terrain-following coordinate system with 21 sigma layers is used, with nonuniform vertical discretization that allows proper resolution of surface and bottom boundary layers. Quoddy uses unstructured meshes of triangles to facilitate variable horizontal resolution. Here, the mesh (Figure 6) provides resolution of order of 1 km along the coast, and grows to roughly 30 km in the deeper water of the GOM. The model has two open boundaries (OBs): one is in shallow water inside the Bay of Fundy, and the other is in the deeper water of the GOM, arching between Cape Cod and Cape Sable. Different approaches are used to specify these two OBs. In the Bay of Fundy, currents are specified with climatological $M_2$ tidal currents [*Lynch et al.*, 1996]. This is justified by the fact that the Bay of Fundy is very shallow, and that $M_2$ tide dominates current and transport variability. Along the seaward OB in the Gulf, the best prior estimation of sea surface elevation at each boundary node is prescribed with climatological $M_2$ tide and residual elevations [*Lynch et al.*, 1996]. This OB is

considered as the active boundary, where sea levels will be adjusted/refined through inverse data assimilation.

[14] To hindcast the coastal circulation, an objective mapping method [*Smith*, 2004] is used to merge CTD measurements with the Gulf of Maine temperature and salinity climatology [*Lynch et al.*, 1996]; together they produce a quasi-synoptic rendition of the shelf hydrography. The forward model Quoddy is initialized with such objectively analyzed temperature and salinity fields, and driven by 6-hourly OI wind fields at the model surface. Observations of surface heat fluxes are not available and thus neglected with the assumption that they play a secondary role (compared with surface wind and offshore boundary forcing) in affecting the coastal circulation dynamics during the 11 days of the field survey. The model is first started on 22 May with the turbulence, velocity and pressure set to zero and temperature and salinity initialized according to the aforementioned objective mapping procedure. After a 2 day integration, wind stress forcing is then ramped up for another 2 days. Model fields at the end of a 4 day spin-up phase are saved as the hot start, which is used as initial conditions to integrate the model forward in time for another 13 days (26 May to 7 June) As a sensitivity experiment, a test run with longer spin-up time (7 days) is carried out. No significant differences in model prior solutions are found. As the model integrates, model prior solutions are compared with in situ current and coastal sea level observations collected between 28 May and 7 June at each individual observational site; misfit between model and data are saved and used subsequently by the inverse models to produce open boundary sea level adjustments. As this is a hindcast, the posterior solution shows misfit at the beginning and throughout the simula-

**Table 1.** Optimal Parameter Used in Inversion of Model Hindcast

| | Parameter | Value |
|---|---|---|
| *Forward Model (Quoddy)* | | |
| Number of vertical nodes | nnv | 21 |
| Forward integration time step | dt | 178.65 s |
| | | |
| *Inverse Models* | | |
| Truxton (tidal band OB elevation inversion) | | |
|   Inverse tidal spectrum | | $M_2$ |
|   Boundary condition size weight | $W_0$ | $10^2$ |
|   Boundary condition slope weight | $W_1$ | $10^{12}$ |
| Casco (Subtidal Band OB Elevation Inversion) | | |
|   Boundary condition size weight | $W_0$ | $10^2$ |
|   Boundary condition slope weights | $W_1$ | $2.6 \times 10^{12}$ |
|   Boundary condition tendency | $W_2$ | $1.8 \times 10^{13}$ |
|   Casco BC temporal resolution | $Tbc$ | 6 hours |
|   Expected velocity misfit | $\sigma_V$ | 0.03 m s$^{-1}$ |
|   Expected elevation misfit | $\sigma_\eta$ | 0.01 m |

tion, smoothed over the time interval. By contrast, a forecast would show low misfit at the start, but growing over time as judged in retrospect.

[15] The inverse models treat tidal and subtidal open boundary sea level inversions separately. This is done by two linear inverse submodels of Quoddy: Truxton [*Lynch et al.*, 1998] and Casco [*Lynch et al.*, 2001], respectively. Truxton is a linear, frequency domain inverse model that uses observations to improve the accuracy of tidal amplitude and phase specifications along the OB. Casco on the other hand is the time domain inverse model that makes use of interior observations to adjust the time-dependent boundary elevations at subtidal scales. At the end of each iteration of the inverse procedure, both tidal (from Truxton) and subtidal (from Casco) elevation adjustments are added to the prior boundary elevations to form more accurate open boundary elevation specifications, which subsequently drive another forward (posterior) model run(from 26 May to 7 June) starting with the hot start mentioned above. Since both Truxton and Casco are linear inverse models of the nonlinear Quoddy model, the inverse solution convergence and thus improvement of boundary elevation specifications requires several iterations of forward/inverse (backward) model runs. Sensitivity tests show that 2 iterations are sufficient in this hindcast.

[16] Mathematically, the inverse is achieved by minimizing a quadratic cost function *J* in the least squares sense. Let η represent the unknown boundary elevation adjustment to be estimated. δ is the velocity data model misfit and ε the elevation misfits. The quadratic cost function *J* is defined as

$$J = \frac{1}{N_\eta \sigma_\eta^2} \sum_{i=1}^{N_\eta} \varepsilon^2 + \frac{1}{N_V \sigma_V^2} \sum_{i=1}^{N_V} \delta^2 + \frac{1}{\int dt} \frac{1}{\int ds}$$
$$\cdot \iint \left[ w_0 \eta^2 + w_1 \left( \frac{\partial \eta}{\partial s} \right)^2 + w_2 \left( \frac{\partial \eta}{\partial t} \right)^2 \right] ds dt$$

where $\sigma_\eta$ and $\sigma_V$ are expected RMS values of misfit ε and δ, $N_\eta$ and $N_V$ are the numbers of elevation and current observations, respectively. *dt* denotes the time interval between 28 May and 7 June, when in situ current and coastal sea level observations were collected, whereas *dS* denotes the spatial interval along the model seaward (active)

open boundary. The elevation boundary condition adjustment η is controlled by regularization terms, where $w_0$, $w_1$, and $w_2$ represent the inverse covariance of the elevation, the elevation slope and the elevation tendency, respectively. Note that Truxton tidal inversion is carried out in the frequency domain, at predefined tidal frequency ($M_2$ in this study). The temporal integration and the $w_2$ term are therefore not applicable in Truxton. It is clear that the inverse procedure requires several parameters: the expected RMS errors of the final misfits $\sigma_\eta$ and $\sigma_V$; the regularization weights $w_0$, $w_1$, and $w_2$, the Truxton tidal spectrum, and the Casco boundary temporal resolution. Criteria on how to optimally choose regularization weights has been derived based on the geostrophic balance and dynamic relation between surface elevation and the wind stress. Interested readers are referred to *Lynch and Naimie* [2002] for detailed description. Derived optimal parameters used in this study are listed in Table 1.

[17] To see how the data inverse improves the open boundary elevation specification, we show in Figure 7 the tidal harmonic constant adjustments produced by Truxton. Comparisons between the prior and posterior indicate the climatological tidal ($M_2$) elevation database [*Lynch et al.*, 1996] is fairly accurate. The tidal band inversion (by Truxton) only produces <3% refinements to the prior $M_2$ tidal amplitude and phase specifications. However it should be noted that the tidal signal is an order of magnitude larger than the subtidal signal. It is found that most of the adjustments are in the vicinity of the Jordan Basin and the Cape Sable. This is the place where both the Scotian shelf water and the deep continental slope water enter the Gulf and can cause seasonal and interannual variability in the local stratification. *Foreman et al.* [1995] reported that uncertainties in the tidal amplitude and phase can appear due to seasonal variability in water stratification. The result here demonstrates that the Truxton tidal band inversion can effectively account for the delicate modulation of the tidal harmonics. Additionally, the short duration of this cruise implies that other much smaller semidiurnal ($N_2$, $S_2$) constituents will be effectively indistinguishable from the dominating $M_2$. The $M_2$ adjustments will be absorbing the spring-neap cycle.

[18] Subtidal sea level adjustment is more important as it determines the subtidal circulation that is often more relevant to the material property transport. Casco provides time-dependent subtidal open boundary sea level adjustments at the specified time interval. For example, a snapshot of the 6-hourly time series of Casco-derived surface elevation at the seaward OB, along with its associated modeled subtidal surface elevation and surface currents is shown in Figure 8. At this particular time, sea level at OB subsides between the Jordan Basin and the Cape Sable with amplitude of about 6 cm. (Note that *Lynch et al.* [1996] estimated sea level variability of o(5cm) along this boundary). The resultant pressure gradient thus drives a cyclonic circulation that is observable in the surface current map (Figure 8, left). The subtidal sea level variation along the OB is a manifestation of the coastal ocean response to remote forcing, including the basin-scale wind and pressure fields, coastal trapped waves, and offshore momentum and buoyancy forcing of upstream Scotian shelf and deep Atlantic Ocean. Previous studies cited earlier [e.g., *Signell et al.*, 1994] emphasize on
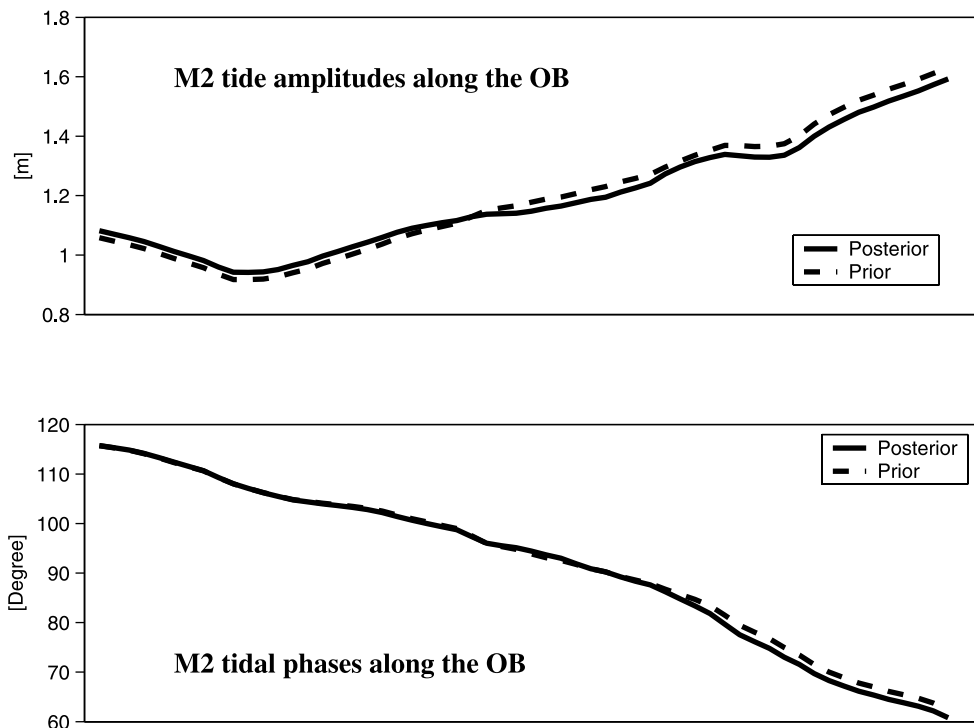
**Figure 7.** M$_2$ tidal amplitude and phase along the model seaward open boundary (from Cape Cod on the left to the Cape Sable on the right). Dashed lines are the prior (climatological) estimates of M$_2$, and solid lines are the posterior (inverted by Truxton).

the necessity of the proper specification of seaward pressure field for a credible regional modeling of subtidal coastal circulation in the GOM. By assimilating interior current and coastal sea level observations, the inverse model Casco is capable of quantitatively specifying subtidal boundary pressure field and thus better accounting for the otherwise unresolved remote forcing influence on the coastal circulation. Interested readers are referred to the Web for an animation showing the complete and quantitative 6-hourly inversion of subtidal boundary elevation, along with its associated modeled surface current and elevation fields (see http://ruoyingh.whoi.edu/MERHAB03/Paper).

## 4. Model Validation

[19] To evaluate the data assimilative hindcast performance, we first compare the modeled and observed coastal sea levels at different tide gauges (Boston, Portland, Bar Harbor, Cutler, and East Port, see Figure 6) along the coast. Note that although coastal sea levels are assimilated into the model hindcast, the variational inverse (rather than direct melding) nature of our approach still warrants detailed examination of the model capability in reproducing the observations. It is seen that the GOM coastal sea levels are dominated by the M$_2$ tide with larger tidal amplitudes in the eastern GOM relative to those in the western GOM (Figure 9). The model is found skillful in resolving the coastal sea level variability, and this is true even for the model prior run that does not include any data assimilations. This is not surprising based on the fact that our prior tidal boundary specifications (using the climatological sea level/tidal database of *Lynch et al.* [1996]) are indeed fairly accurate (i.e., Figure 7). Adding

data assimilation further improves the model performance as demonstrated by systematic reductions of sea level RMS misfits after each forward/backward iteration. As a result, averaged over all 5 coastal stations, the mean sea level RMS difference between model posteriors and observations is only 8.22 cm (relative to $2-3$ m coastal sea level variations).

[20] Important value of data assimilation is further revealed after coastal sea level time series (both observed and modeled) are detided by low-pass filtering (Figure 10). Compared to tidal sea level, subtidal sea level is much smaller in amplitude ($0.10-0.15$ m) at each station. It is more striking to see that without data assimilation, the model prior solutions are incapable of getting the subtidal sea level correct. As discussed earlier, subtidal sea level variations in the GOM are related to the larger-scale pressure fields and dynamics such as the propagation of coastal trapped waves. Without proper specification of upstream sea level (pressure) condition, our regional circulation model cannot reproduce observed dynamic responses. By assimilating in situ coastal sea level and current observations, the inverse data assimilation models capture the missing dynamics at the open boundary in a dynamically consistent and quantitatively accurate manner, and thus allow improvements in model simulations and model and data comparisons. Data assimilation also improves the accuracy of the modeled current fields. The overall RMS misfit between the modeled and observed depth-averaged currents is reduced by 10% between the prior and posterior runs. While this improvement in depth-averaged currents may seem modest, there are several points to keep in mind.

[21] First, the ADCP velocity data are intrinsically 'noisy'. The important subtidal motions are only $10-30\%$
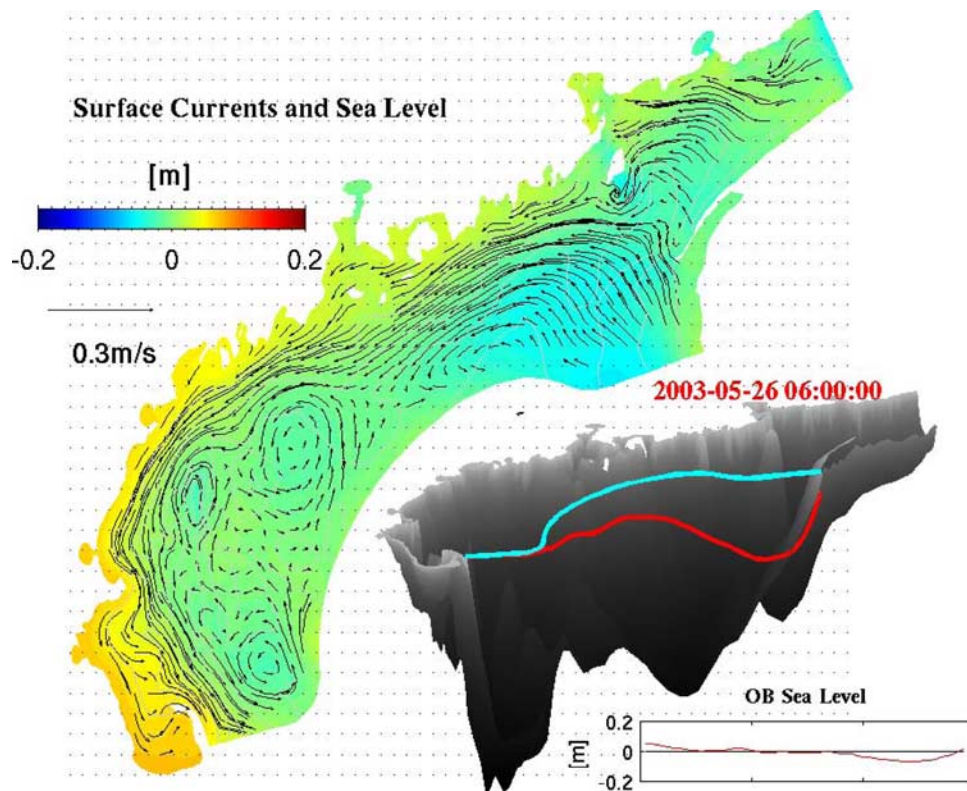
**Figure 8.** A snapshot of the subtidal sea level (inverted by Casco, denoted by red curve) at the model seaward open boundary along with the modeled subtidal surface elevation and surface current at this particular time. Note that the blue curve overlaid on the 3-D bathymetry indicates the location of model seaward open boundary, and the open boundary sea level (red curve) on the same plot is exaggerated to show its spatial pattern. The real value of OB sea level is shown in the bottom right, where the left (right) end of the x axis is Cape Code (Cape Sable).

of the whole signal, which includes a strong tidal component. Additionally, velocity data are sensitive to unresolved local topographic influences – both tidal and subtidal. All velocity measurements will be unpredictably biased by this effect. Measurement on a moving platform (ship) converts most of this bias into 'noise', obscuring the underlying signal. Fixed stations will retain the topographic bias, unless by averaging misfits over several stations we effectively convert the bias to noise. In either case, a fixed improvement in skill will appear less important relative to the signal, as the noise level increases.

[22] Second, the prior (in particular the tidal band) is very good in this case. It is forced by spatially varying OI wind, and by a good prior estimate of the open boundary conditions. In the latter, the primary deficit is the wind-related pressure signal; the tidal adjustment mentioned above may be of comparable size.

[23] Third, data assimilation has the potential to "chase noise". For example, the model will fit the noisy data better if more freedoms are allowed to perturb boundary sea levels. This can help improve fitting of noises, but not necessarily the overall quality of model solutions. Apparently this is not the case here; rather that degrading the solution falsely, it is improving it.

[24] Last, which is shown in section 5, the posterior misfit in the assimilated velocity data is much larger than that of the unassimilated Lagrangian drifter trajectories (the

Lagrangian misfit being an integral of Eulerian misfit). This fact supports above interpretations about the noisy nature of current data.

[25] During the field survey, a total of 6 satellite-tracked drifters were released along the easternmost transect (VI in Figure 2). Among them, the most onshore release was a surface drifter. The rest were drogued at 15 m below the surface. Since the drifter trajectory information has not been assimilated, collectively, they not only provide useful observations as to where the material property may have been transported by the coastal current, but also act as independent data sets to evaluate the skill of the data assimilative hindcast. To do that, numerical particles are released at the same time, location and water depth of each drifter deployment and are tracked simultaneously as the model hindcast integrated forward in time. The numerical particle tracking starts from 31 May (year day 151) when the drifters were released to 7 June (year day 158) when the field survey completed. During this 7 day tracking period, the modeled and observed drifter trajectories in general stay in track to each other (Figure 11), both exhibiting significant spatial displacements as a result of the MCC transport. The complexities in temporal and spatial structures of drifter tracking are clear. For the first 1.5 days following drifter deployment on 31 May, divergence of all six drifters (Figure 12) grows linearly in time. Note that this time period partially overlaps with a strong downwelling wind
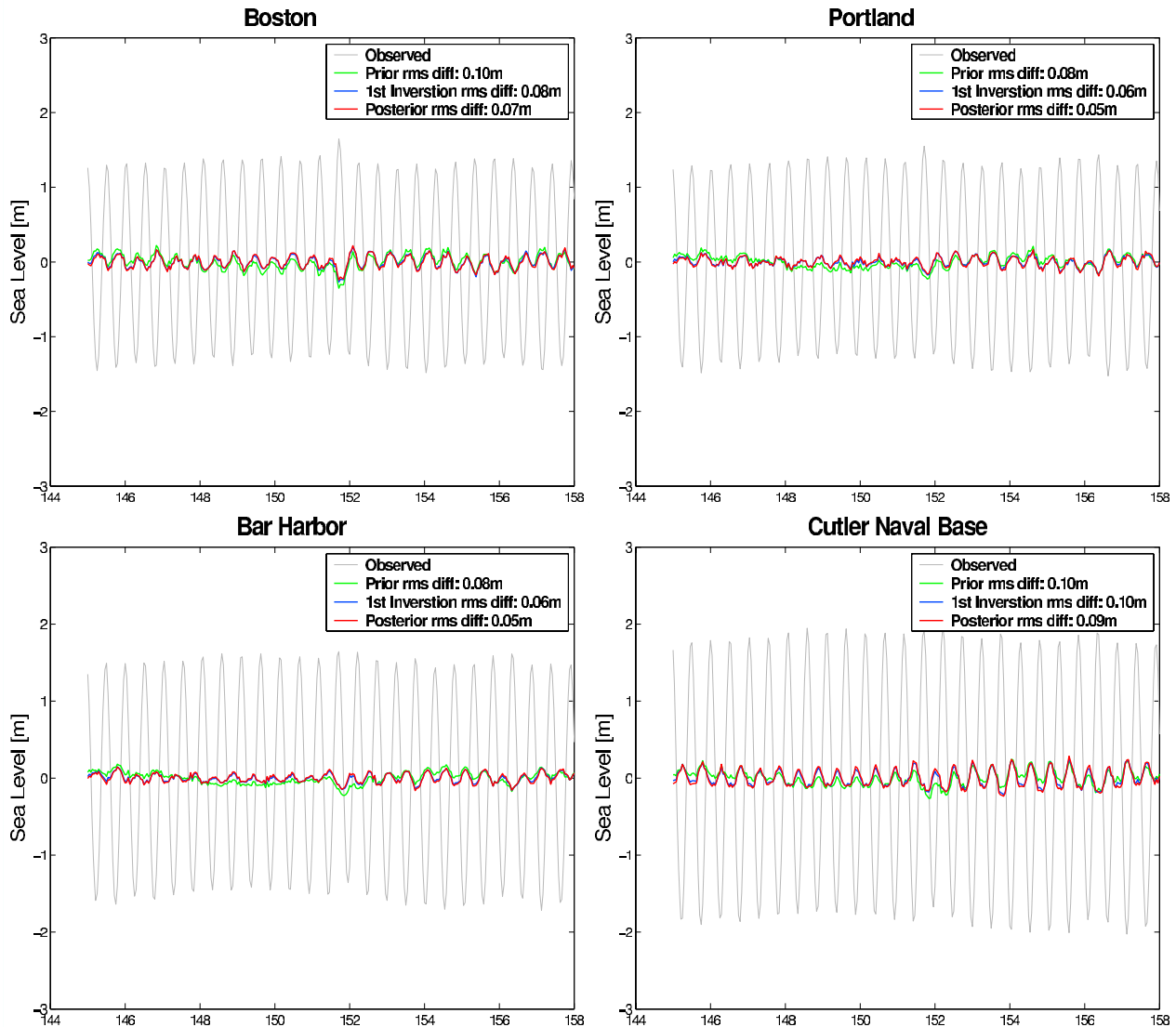
**Figure 9.** Observed sea levels and misfits between observed and modeled sea levels at Boston, Portland, Bar Harbor, and Eastport. In each panel, observations, misfits between data and prior model solutions (no data assimilation), misfits between data and the forward model solutions (after first forward/ inverse iteration), and misfits between data and posterior model solutions are indicated by gray, green, blue, and red, respectively.

event that occurred on 1–3 June (Figure 4). Subsequently, growth of the divergence lessens, with some of the simulated drifters actually drawing closer to observations than they were before. To quantify the model ability in tracking drifter trajectories, the time series of modeled and observed drifter divergence is produced (Figure 12), along with the mean drifter divergence rate calculated by averaging divergence of all six drifters/numerical particle pairs. The resulting mean divergence rate is found to be 1.78 km d$^{-1}$, equivalent to a RMS Eulerian current error of about 0.02 m s$^{-1}$ Considering the background MCC is of $\sim$0.2–0.3 m s$^{-1}$, we conclude the present data assimilative hindcast has decent tracking skill. Note that in previous Georges Bank data assimilation experiments when only shipboard ADCP currents were assimilated, the mean trajectory divergence rate was found to be 3.4 km d$^{-1}$ in *Lynch et al.* [2000] and 2.4 km d$^{-1}$ in *Aretxabaleta et al.*

[2005], respectively. The result here is therefore an encouraging improvement.

[26] In the particle tacking mentioned above, we only consider advection by the model currents without modeling turbulent dispersion and diffusion explicitly. The true velocity field $U_T(x, t)$ in fact contain both deterministic and stochastic parts: $U_T(x, t) = \overline{u}_T + \hat{u}_T$. In the absence of subgrid-scale turbulent processes, the modeled drifter velocity $U_M$ has only a deterministic part:

$$U_M(x, t) = \overline{u}_M$$

Lagrangian integrals of these motion fields produce true and modeled displacements

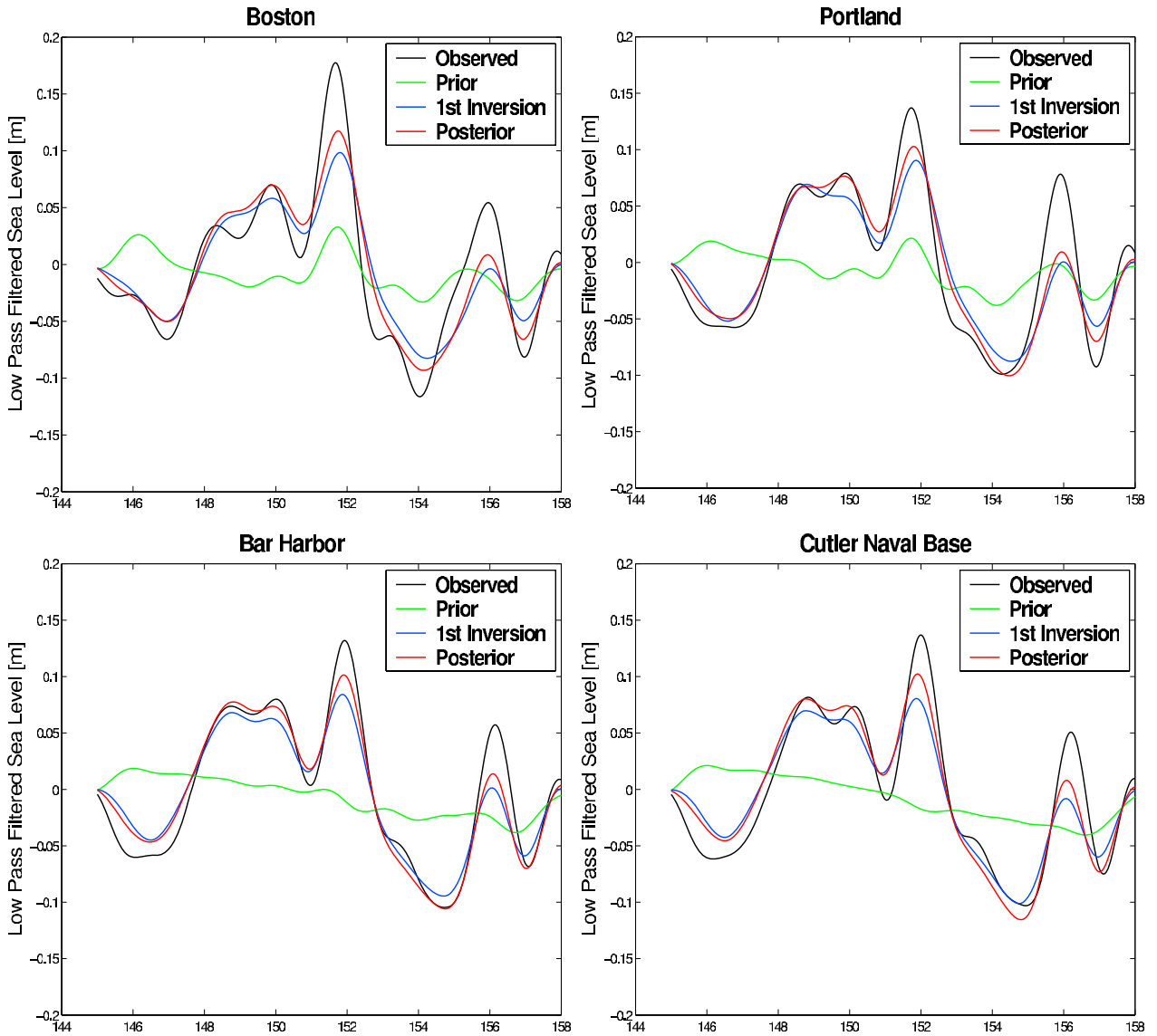$$X_T(t) - X_T(0) = \int_T (\overline{u}_T + \hat{u}_T)dt$$

**Figure 10.** Observed and modeled 36 hour low-pass-filtered coastal sea levels at Boston, Portland, Bar Harbor, and Eastport. In each panel, observations, prior model solution (no data assimilation), the forward model solution (after first forward/inverse iteration), and the posterior model solution are indicated by black, green, blue, and red, respectively.

and

$$X_M(t) - X_M(0) = \int_M \overline{u}_M dt$$

where $\int_T$ and $\int_M$ indicate the path integral. If assuming identical starting points ($X_T(0) = X_M(0)$) and ignoring the difference between $\int_T$ and $\int_M$, we have the drifter divergence $\boldsymbol{X(t)}$:

$$X(t) = \int_T (\overline{u}_T + \hat{u}_T) dt - \int_M \overline{u}_M dt = \int \overline{\varepsilon} dt + \int_T \hat{u}_T dt$$

where $\overline{\varepsilon}$ is deterministic misfit velocity. If the modeled current is accurate (i.e., $\overline{u}_T = \overline{u}_M$, $\overline{\varepsilon} = 0$), the drifter

divergence $\boldsymbol{X}$ is then the result of turbulent flow and corresponds to the single particle dispersion due to the turbulent motions. *Taylor* [1921] shows that in steady and homogeneous turbulence the particle dispersion (divergence) function would change from a straight line (proportional to the time) for a short period in the beginning to a parabolic curve (proportional to the square root of time) at a later time. However, the Taylor dispersion theory is invalid in real coastal ocean as motions are neither steady nor homogenous. This is demonstrated by the general reduction in particle divergences seen in Figure 12 after ~1.5 days, as opposed to continue increasing over time, albeit at a slower rate, predicted by the Taylor theory. Whether or not these findings are specific to this particular ensemble of drifters is not known, nor is it clear how to partition the divergence between its deterministic and
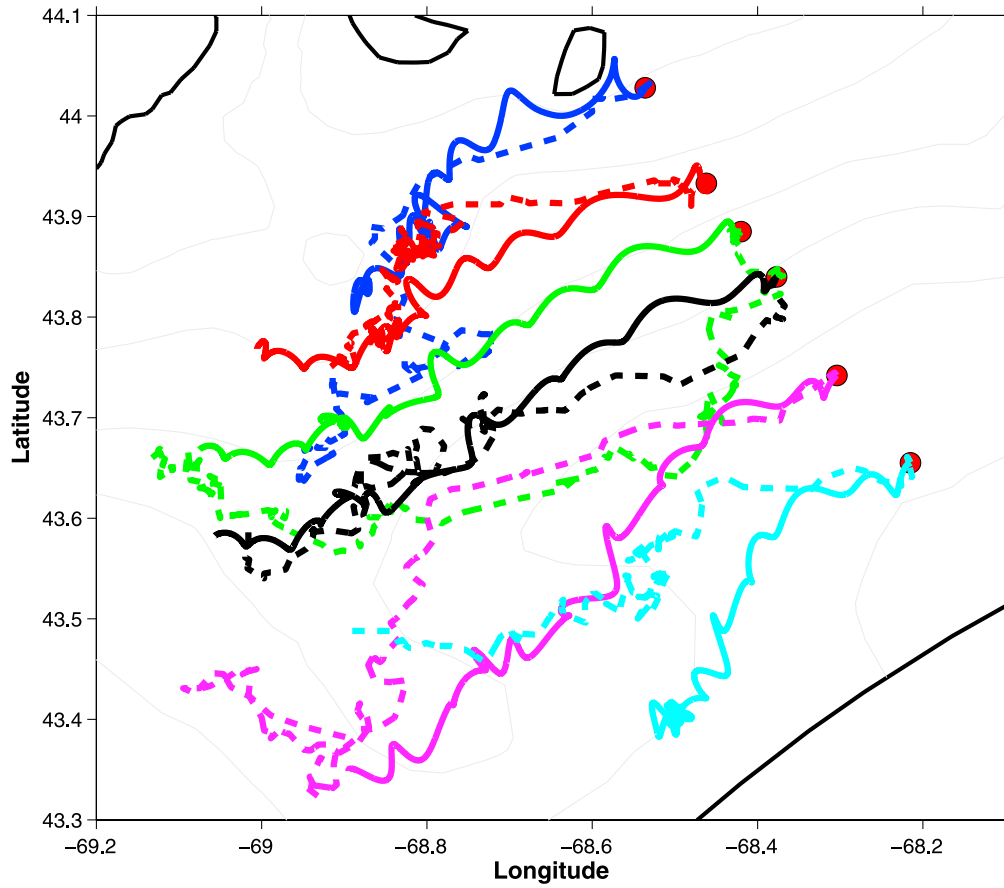
**Figure 11.** Comparisons between the modeled (solid lines) and observed (dash lines) drifter trajectories. Release at most onshore location was a surface drifter, and the rest were drogued at 15 m.
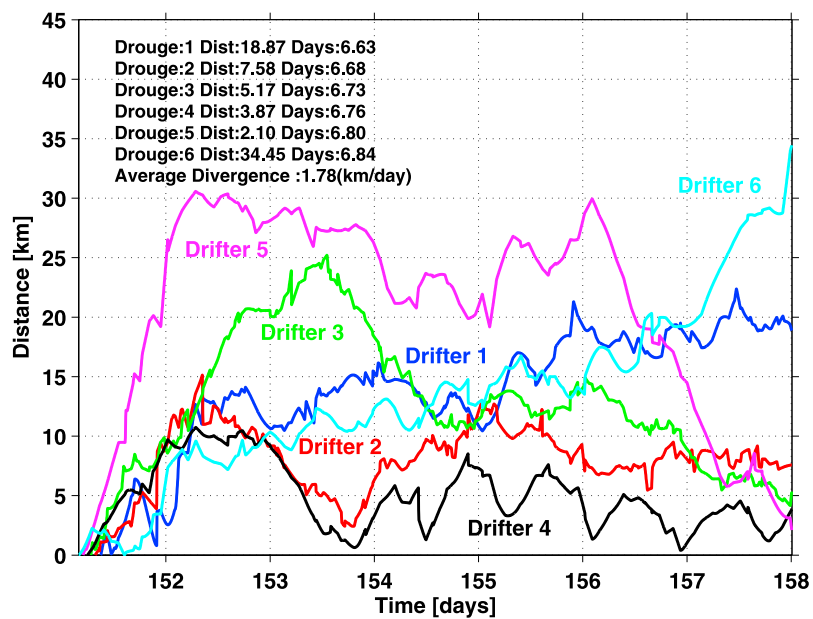


**Figure 12.** Time series of divergence between modeled and observed drifter trajectories.
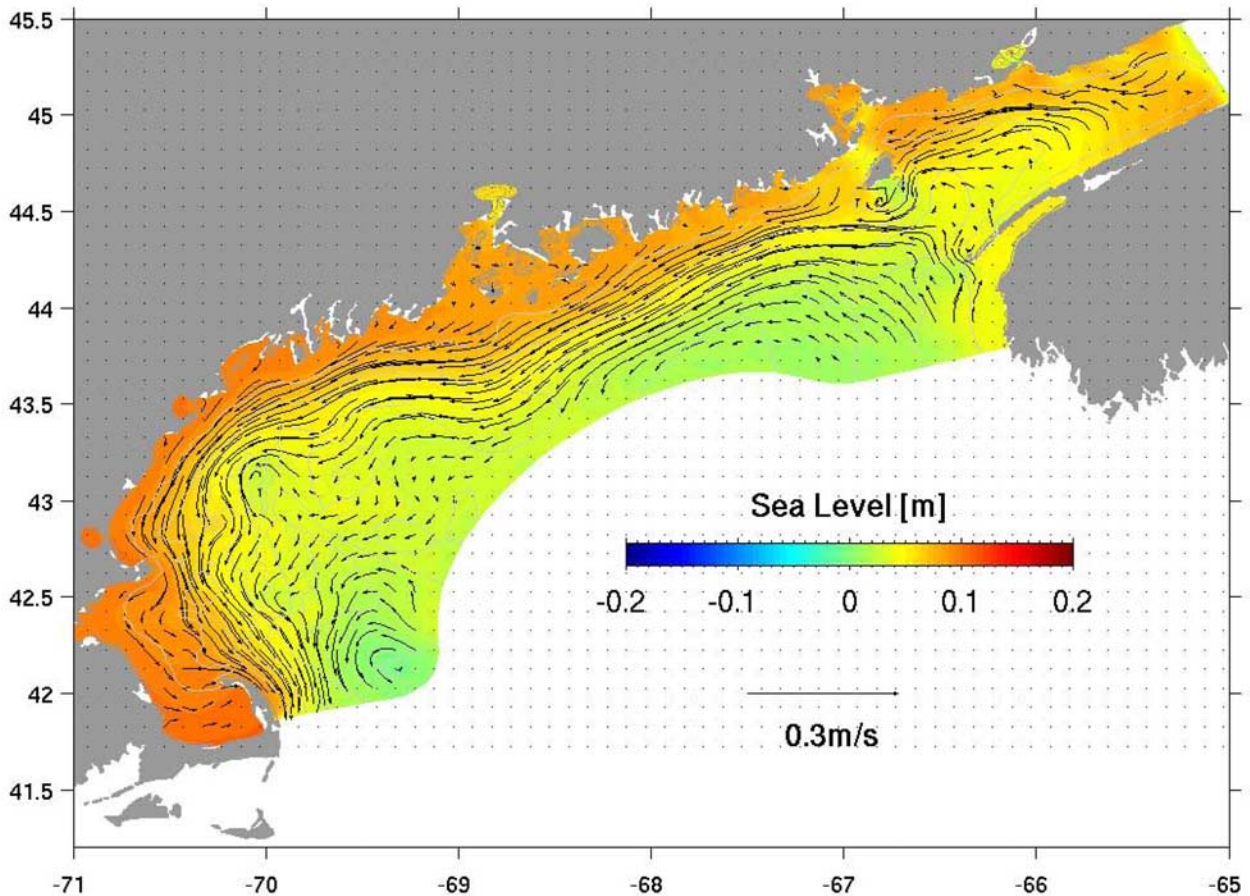
**Figure 13.** Temporal means (averaged between 25 May and 7 June) of sea level and surface currents in the Gulf of Maine.

stochastic components. Further research on this topic utilizing larger ensembles is clearly needed.

## 5. Subtidal Model Solution

[27] Data assimilative model solutions at the subtidal timescale are examined in detail in this section because subtidal coastal circulation driven by wind, density and offshore low-frequency forcing, plays an important role in coastal water property transport. We here focus on the data assimilative model solutions between 25 May and 7 June, a 13 day period encompassing the field survey. To remove the tidal effect, each of the model state variables is averaged over the $M_2$ tidal period (12.42 hours), resulting for each variable a time series of 26 snapshots of subtidal model solutions.

### 5.1. EOF Analysis

[28] The temporal and spatial variability of data assimilative model hindcasts of surface elevation $\eta$ and surface current $(u, v)$ are first examined by decomposing them into EOFs. By organizing $A$

$$A = \begin{pmatrix} \eta \\ u \\ v \end{pmatrix}$$

in an M × N matrix, where M and N represent the spatial (6672 × 3 grid points) and the temporal (26 semidiurnal averages between 25 May and 7 June) elements, respectively, matrix $A(x, y, t)$ may be represented by

$$A(x, y, t) = \sum_{n=1}^{N} a_n(t) F_n(x, y)$$

where the $a_n$ are the temporal evolution functions and $F_n$ are the spatial eigenfunctions for each EOF mode, respectively. Figure 13 shows temporal means of sea level and surface currents, which indeed ensemble known seasonal features of gulf-wide sea level (pressure) and circulation distributions (e.g., cyclonic MCC). Prior to the EOF analysis, these temporal mean fields are removed from $A$ so that the synoptic variability can be extracted from the background mean fields.

[29] The first EOF mode (Figure 14) accounts for 47% of the total variance. The first mode eigenfunction (upper left panel) indicates sea level rise along the western GOM, as a consequence of onshore moving (downwelling type) surface currents. The temporal evolution function is found negatively correlated with surface winds with positive (negative) perturbation during downwelling- (upwelling) favorable wind events (lower right two panels). The correlation
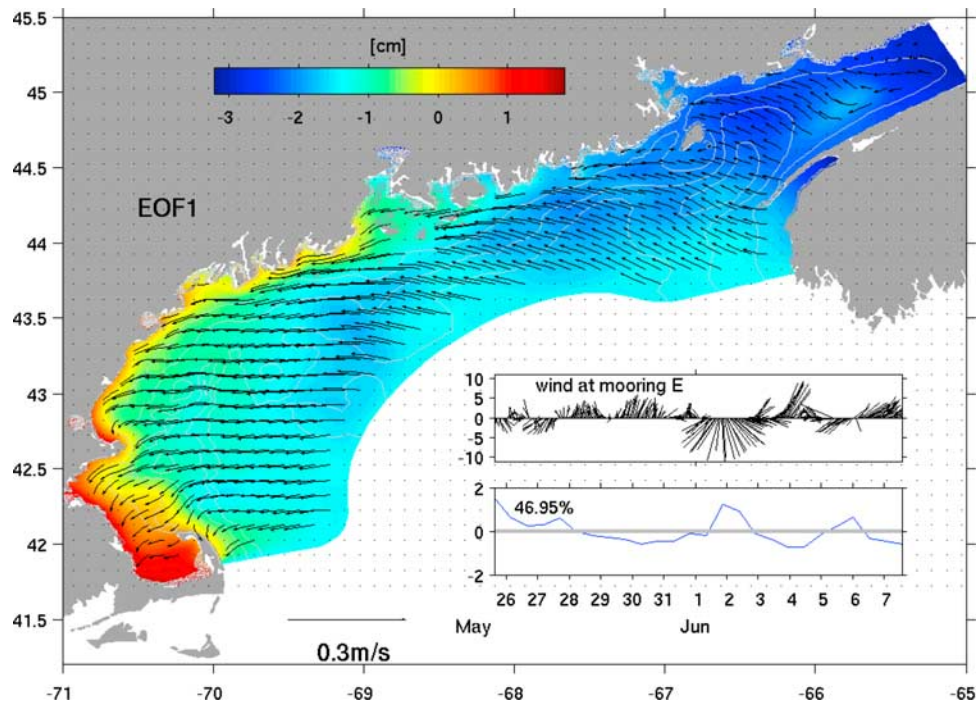
**Figure 14.** Eigenfunction and temporal evolution function for the first EOF mode. The color panel and vector plot are the orthogonal spatial eigenfunctions of surface elevation and surface currents that contain the physical units. The time series are their respective orthonormal temporal evolutions functions (bottom inset) along with the de-meaned 36 hour low-pass-filtered wind vectors observed at GOMOOS mooring E (top inset).

coefficient *r* between temporal evolution function and the alongshore component of wind is −0.72, suggesting surface wind forcing is the responsible dynamic factor for this EOF mode. Given that the overall mean of the temporal evolution function is positive, this mode indicates that the coastal ocean variability during the study period is dominated by the downwelling circulation. It is also noted that the rising sea level in the Massachusetts Bay is capable of setting up the alongshore pressure gradient between the eastern and the western GOM. This gradient has notable effect on the alongshore current and transport, as will be shown later.

[30] The second EOF mode (Figure 15) accounts for 22% of the variance. The second mode eigenfunction (upper left panel) exhibit the set down of sea level and offshore-moving surface currents. Compared to the first EOF mode, the temporal evolution function of this mode is not as well as correlated with the surface wind (lower right two panels of Figure 15). The correlation coefficient *r* between temporal evolution function and the alongshore component of wind is only −0.28. During the strong downwelling-favorable wind event between 1 and 3 June, wind directions changed from southwestward to south and southeastward. In response, the temporal evolution function changes from negative perturbation to positive perturbation, suggesting coastal currents change from onshore direction (downwelling type) to offshore direction (upwelling type). This highlights the fact that due to the complex coastline geometry, coastal ocean response is often determined by subtle changes in the relative orientations between the coastline and the wind direction.

[31] The third EOF mode (Figure 16) accounts for 8% of variance. Here, the eigenfunctions (upper left panel of

Figure 16) reveals some sea level variations along the model seaward boundary in the vicinity of Jordan Basin and Cape Sable, probably related to deep ocean forcing. Some mode structures are also seen near major topographic settings inside the Gulf, possibly the result of topographic steering effects; although these interpretations must be tempered since this mode only contains less than 10% of the total variance.

[32] In total the first three EOF modes account for 77% of surface variance. With 23% of variance remaining in higher modes a reconstruction of the surface fields to account for the synoptic-scale variability would require several more modes.

## 5.2. Across-Shelf Transects

[33] Temporal means of alongshore velocity, across-shelf velocity, vertical velocity and temperature are sampled along transects I–VI (Figure 2) between the Penobscot and Casco bays. At all 6 transects (Figure 17), alongshore mean velocities are characterized by a southwestward coast jet with a speed of ~0.15 m s$^{-1}$. This is the MCC that passes through the area and transports cold and nutrient rich water from Bay of Fundy and the Eastern GOM to the western GOM. The current magnitudes in the middle portion (e.g., transect IV) of the region are smaller than their counterparts in the east and west as the result of divergence of local bottom bathymetry. Here currents are steered offshore with their intensity in the alongshore direction reduced. Near the bottom of the westernmost (transects I, II and III) transect, we see a countercurrent moving toward northeast. This current is related to the alongshore pressure gradient setup demonstrated earlier in Figure 14. Similar alongshore
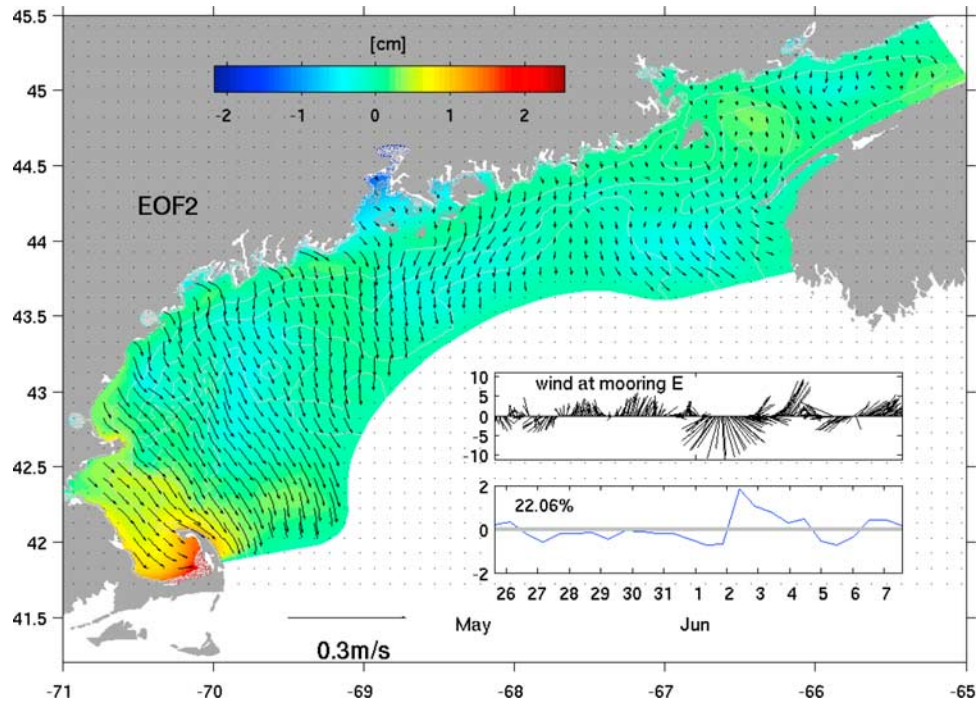
**Figure 15.** Same as Figure 14, except for the second EOF mode.

pressure-driven countercurrent is not atypical, and has been observed in other coastal regions including California coast and the west Florida shelf. The mean across-shelf velocities (especially at transects I, II, III and IV) are moving onshore. This is consistent with Ekman dynamics and earlier finding that the mean wind forcing during the study period is downwelling-favorable. These mean across-shelf currents are about $0.02–0.04$ m s$^{-1}$, suggesting a 2–4 km d$^{-1}$ net onshore transport. Onshore transport at the surface often-times is associated with offshore transport near the bottom. Such two-layer structure is most clearly seen at transect I.

[34] Along all 6 transects vertical velocity $w$ (calculated in a way consistent with *Luettich et al.*'s [2002] method) exhibit rich spatial structures. Although downwelling favor-able wind dominates during the survey period, positive vertical velocity $w$ (upwelling) at various potions of these
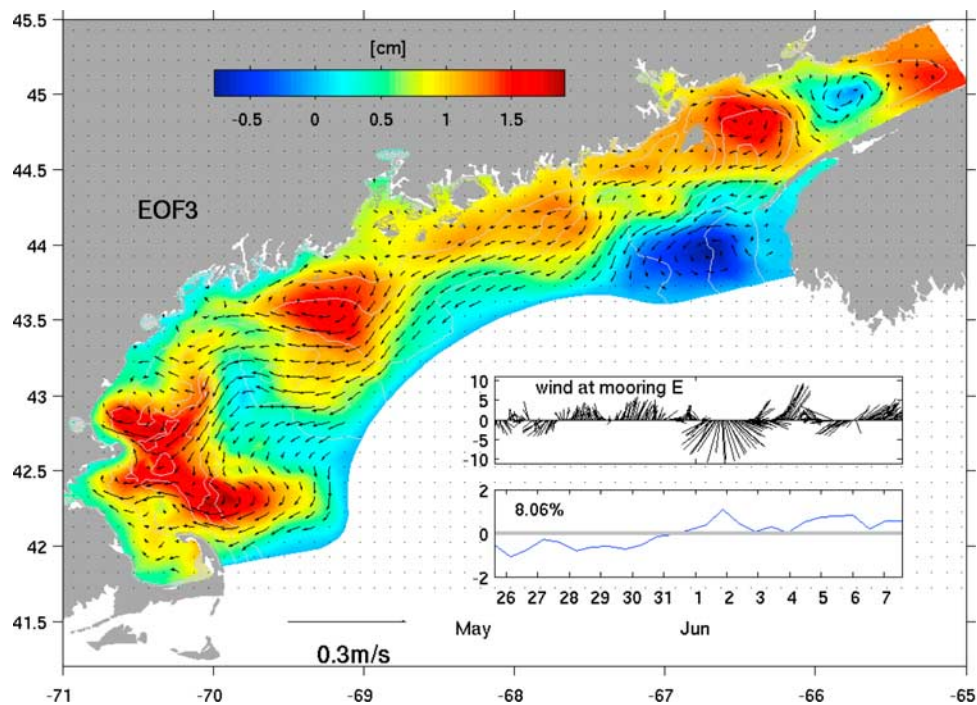


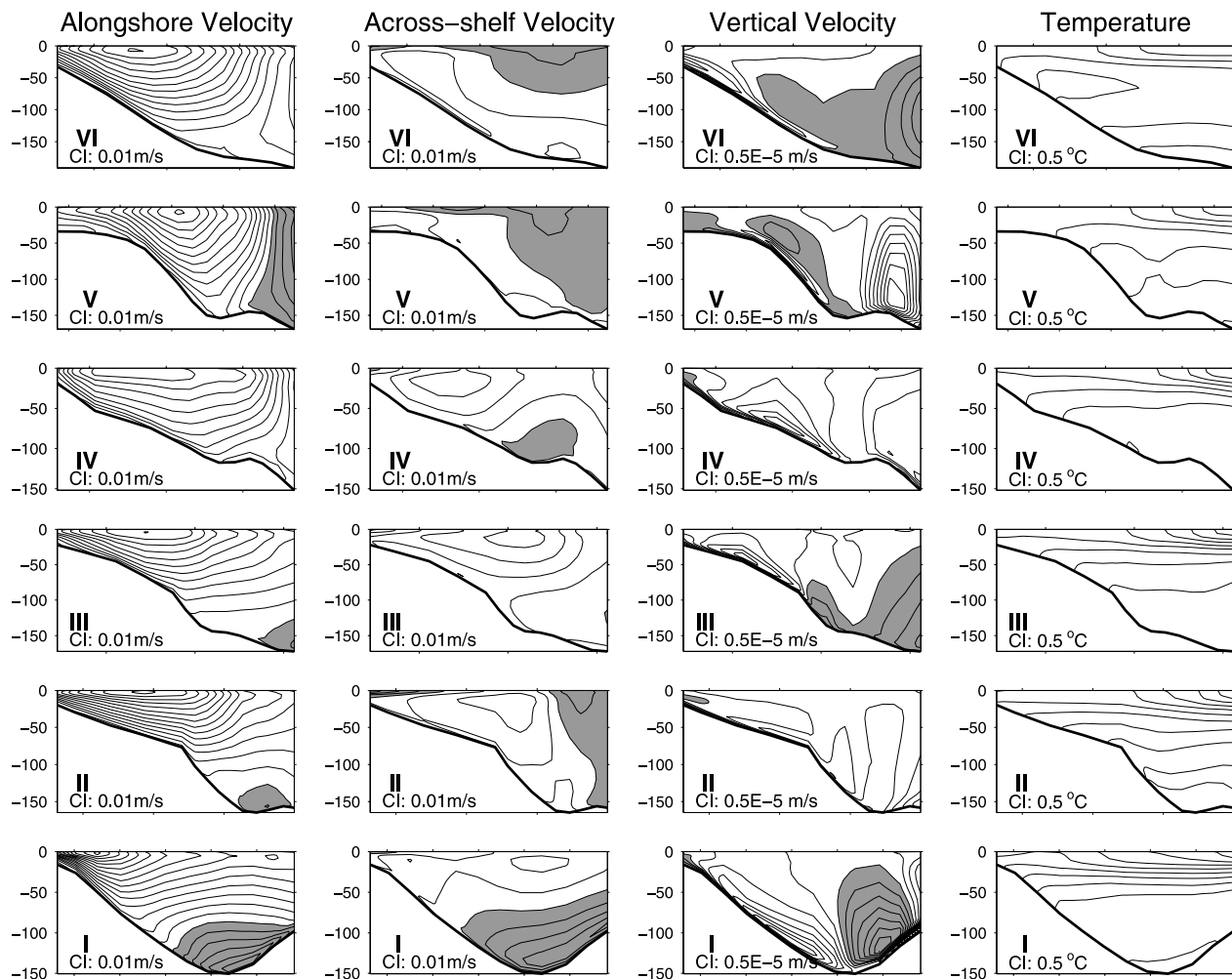**Figure 16.** Same as Figure 14, except for the third EOF mode.

**Figure 17.** Temporal means (averaged between 25 May and 7 June) of subtidal alongshore velocity, across-shelf velocity, vertical velocity, and temperature sampled along six transects of the field survey (Figure 2). The right-hand Cartesian coordinate system is used, so positive contours (shaded areas) indicate northeastward alongshore current/offshore moving across-shelf current/upward moving vertical velocity.

transects are seen. In particular, the mean upwelling vertical velocity at transect I is about $4 \times 10^{-5}$ m s$^{-1}$, equivalent to a 4 m d$^{-1}$ net upwelling transport. This is significant considering the local water depth is only about 120 m. Across-shelf mean temperature transects also reveal an alongshore temperature gradient between the eastern and the western GOM. Stronger tidal mixing stirs up coastal water in the eastern GOM. Consequently, waters in the western GOM are more stratified compared with those in the eastern gulf.

### 5.3. Bottom Currents

[35] Presumably, the GOM Harmful algal (*A. fundyense*) blooms that populate in this coastal current originate from germinated cysts. One hypothesis is that the algal cells might emerge from a large, offshore cyst accumulation in the bottom of coastal water offshore of Casco and Penobscot bays [*McGillicuddy et al.*, 2003; *Anderson et al.*, 2005; *McGillicuddy et al.*, 2005]. It is therefore of interest to examine in detail the coastal current structures near the bottom offshore of Penobscot and Casco bays. Subtidal

mean bottom currents (Figure 18) averaged over the study period (25 May to 7 June) show many small-scale eddy structures, indicating that bottom circulation and the associated material transport are complicated in nature. There is a weak flow convergent zone in the middle between Penobscot and Casco bays, where the westward flowing bottom currents meet the countercurrents moving eastward. Potentially, this provides a mechanism for local accumulations of material properties (not limited to cysts only). Whether or not they can move to the surface depend upon their buoyancy and/or swimming abilities as well as local upwelling and downwelling dynamics.

[36] Temporal mean (over the same 25 May to 7 June period) of subtidal bottom vertical velocity (Figure 19) identifies several upwelling and downwelling centers (annotated in Figure 19). These upwelling and downwelling centers are located in the offshore deep water, and are thus not directly related to surface wind fields. When examining them together with the fine structures of local bathymetry, we see that most of upwelling/downwelling centers are located in the vicinity of significant topographic variations
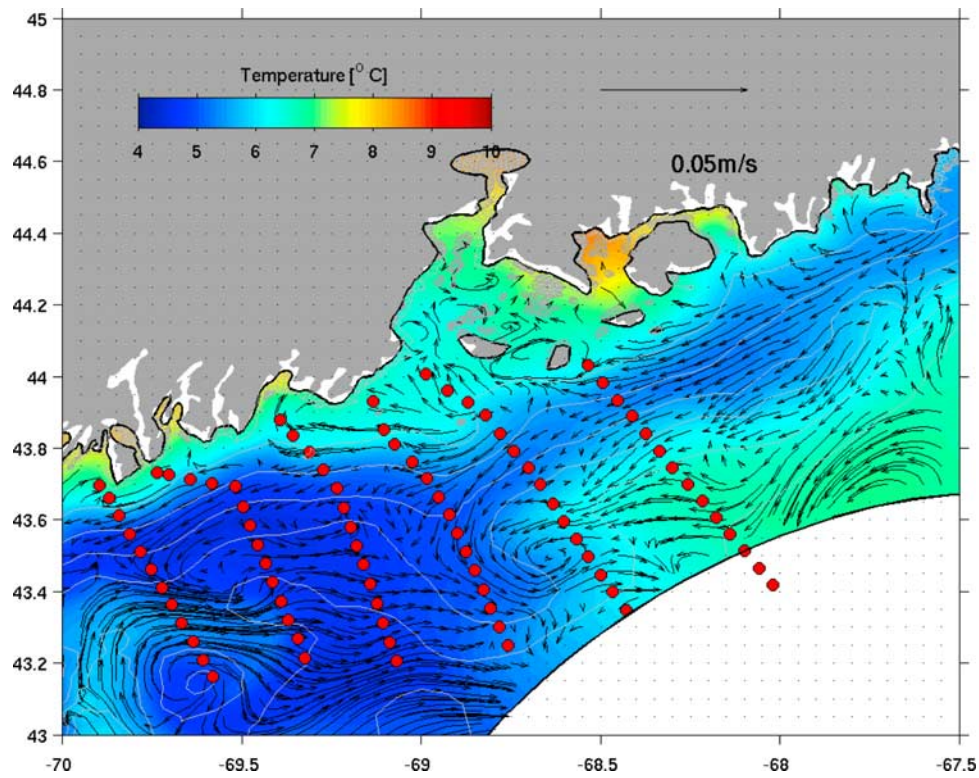
**Figure 18.** Temporal means (averaged between 25 May and 7 June) of subtidal bottom currents and bottom temperature, overlaid by CTD stations and bathymetric contours.
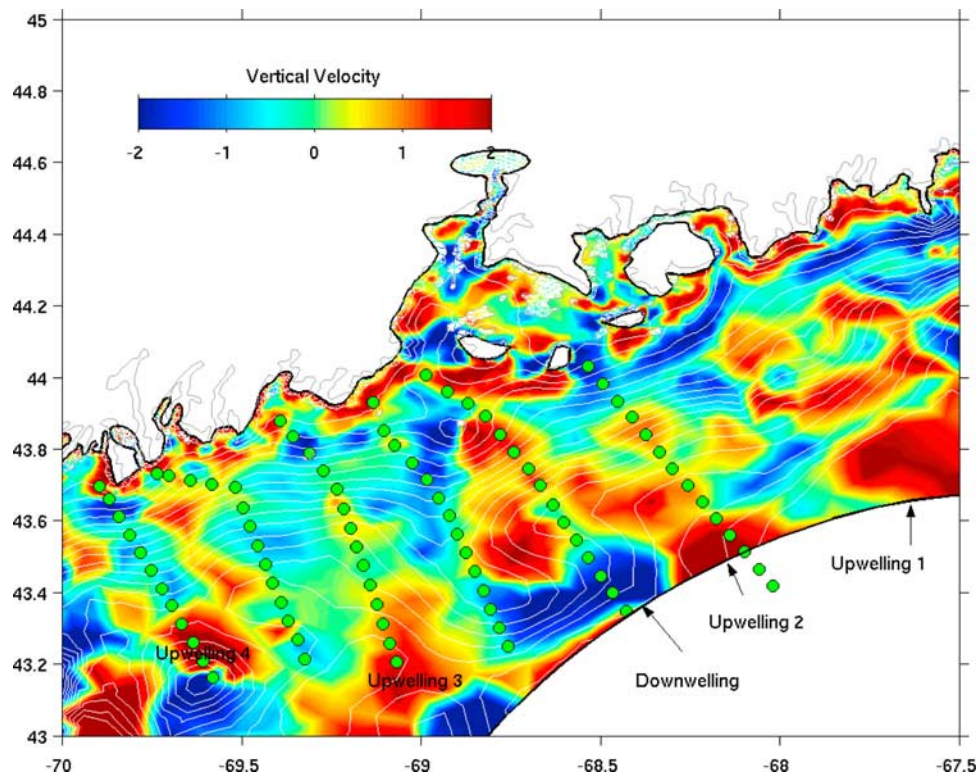


**Figure 19.** Temporal mean (averaged between 25 May and 7 June) of subtidal bottom vertical velocity, overlaid by CTD stations and bathymetric contours. Unit of the color bar is $10^{-5}$ m/s.

**Table 2.** Sensitivity Model Experiments and Results

| Model Experiment | In Situ Data Used for Inversion | Surface forcing | Drifter Trajectories Mean Divergence, km d$^{-1}$ | Overall Sea Level RMS Misfit, cm | Overall Current RMS Misfit, cm s$^{-1}$ |
|---|---|---|---|---|---|
| Prior | no data inversion | OI wind | 2.27 | 11.23 | 9.07 |
| Case I (central hindcast) | coastal sea levels plus ADCP currents | OI wind | 1.78 | 8.22 | 8.18 |
| Case II | coastal sea levels plus ADCP currents | 1 point wind | 1.90 | 8.36 | 8.32 |
| Case III | ADCP currents only | OI wind | 1.99 | 10.10 | 8.20 |
| Case IV | coastal sea levels only | OI wind | 2.59 | 8.49 | 10.81 |
| Case V | coastal Sea Levels plus ADCP currents | OI wind (includes QuikScat scatterometers) | 1.49 | 8.02 | 7.88 |

(such as upwelling centers 1, 2, 3, and 4). These bottom vertical currents are in fact determined by the kinematic boundary condition such that $w = -uh_x - vh_y$. For instance, what happens at transect I (Figure 17) is that the offshore-moving bottom current ($u > 0$) run into a shallow bank ($h_x < 0$). Collectively, they produce the positive (upwelling) vertical velocity as seen along the offshore portion of this transect. Similarly, when negative (southwestward) alongshore coastal currents (v < 0) pass through certain locations that have positive topographic change ($h_y > 0$), positive vertical currents (upwelling) are generated, and vice versa. Therefore, by obeying fluid continuity and kinematic condition, the complex coastal currents in connection with complex bathymetric structures offshore of the Penobscot and Casco bays are capable of constantly generating many local upwelling and downwelling centers. Such small-scale bathymetric structures and 3-D hydrodynamics may play important roles in local plankton dynamics, and warrant detailed examinations that combine more field data with numerical model experiments.

## 6. Sensitivity Experiments

[37] To see if either ADCP currents alone or coastal sea levels alone could achieve the same model skill presented above, we perform several sensitivity experiments and compare them with the prior model run that does not include any data assimilation. Case I is the model hindcast presented above (central hindcast), which takes OI surface wind fields and assimilates both coastal sea level and depth-averaged current measurements. To see whether the model simulation driven by the OI wind fields performs any better than a simulation driven by a single point wind measurement, a twin experiment case II is run with spatially uniform winds (observed at GOMOOS mooring E). Case III, as previous data assimilative modeling studies on the Georges Bank, only assimilates moored and shipboard ADCP currents; in contrast, case IV only assimilates coastal sea levels. Finally, case V is constructed identically as case I (central hindcast) except that the surface wind OI procedure now also includes additional, independent GOM wind observations (25 km resolution) from the satellite QuikScat scatterometer, which has be shown to produce accurate wind measurements in the coastal ocean [*Pickett et al.*, 2003]. For the sake of scope of this paper and brevity, we leave detailed descriptions of this experiment to a separate, future correspondence and simply cite its results here so to compare with other sensitivity experiments. The skill of

each individual model run is evaluated by the mean divergences of modeled and observed drifter trajectories, along with overall RMS misfits between the modeled and observed sea levels and depth-averaged currents. These sensitivity experiments and results are summarized in Table 2.

[38] All sensitivity experiments, including the prior model run that does not include any data assimilation, produce good model skill in term of the mean divergence. Relative to the prior, Case I (central hindcast) shows that adding current and sea level data assimilation improves the model drifter prediction accuracy by 22% and reduces RMS misfits of sea level and depth-averaged currents by 27 and 10%, respectively. Compared with case I, case II has degraded model skill, indicating the spatial variability in the wind field is an important factor that needs to be accounted for. Case III considering only currents assimilation shows some further skill reductions in drifter tracking. Moreover, without coastal sea level assimilation, the modeled and observed sea levels comparisons degrade too, suggesting assimilation of offshore currents in the a limited coastal region (between Penobscot and Casco bays) alone is not sufficient to account for sea level variability along the coast. Considering only coastal sea level assimilation, case IV as expected provides better coastal sea level fits than the prior. However, without constraints from offshore velocity observations, the model fits to the ADCP data is degraded with respect to the central hindcast. Since most of our drifters are offshore, the resulting degraded offshore currents consequently produce the largest drifter divergence (even worse than the prior). This implies that offshore observations are necessary components of coastal ocean data assimilation. Finally, case V shows the most superior model performance among all in terms of the model/data misfits of drifter divergence, sea levels and currents. This is achieved by including independent satellite QuikScat wind observations into the OI, demonstrating the utility of QuikSCAT scatterometer data in further improving coastal wind field specifications, and thus ocean model realizations of coastal circulation and material property transport. Overall, the best assimilation strategy is to use the best possible forcing fields and assimilate both offshore ADCP currents and coastal sea levels so that collectively they provide constraints from point and field measurements with more spatial and temporal coverage for both coastal and offshore water. After all, for any data assimilation application, the more independent and high-quality in situ observations, the more valid data constraints imposed on the

dynamic model, and the more accurate data assimilative model solutions we can achieve. One caveat in sensitivity experiments discussed here is that we used the same set of inversion parameters (Table 1). These parameters are estimated from the data with the criteria of *Lynch and Naimie* [2002]. More experiments may be needed in the future to explore model solution sensitivity to theses parameters.

## 7. Summary and Conclusion

[39] Both coastal sea levels and depth-averaged currents are assimilated into the model hindcast in this study. This is different from previous data assimilation modeling experiments [*Lynch and Hannah*, 2001; *Manning et al.*, 2001; *Lynch and Naimie*, 2002; *Aretxabaleta et al.*, 2005] where only depth-averaged shipboard ADCP currents were assimilated. The sensitivity experiments presented here demonstrate the importance of using both.

[40] The open boundary sea level inversion strategy used here has been successfully applied in previous circulation studies on the Georges Bank. By implementing it in the dynamically more diverse GOM coastal ocean in this study, we demonstrate its utility for a general coastal setting. Admittedly, we benefit from previous research in GOM circulation modeling, and excellent databases of tides and hydrographic climatology [*Lynch et al.*, 1996], which enable us to start this data assimilation application with an excellent prior estimation. Further improvement of our model skill may be achieved by including surface heat fluxes and other tidal constituents into the model calculations.

[41] The underlying assumption applied in current inverse strategy is that model/data misfits are the result of inaccurate specification of barotropic sea levels at the open boundary. This is justified by the fact that in the GOM, barotropic sea levels in both tidal and subtidal bands are the biggest contributors to model/data misfit and also the principle unmeasured boundary conditions. In term of baroclinic adjustment at the boundary, many other factors (e.g., stratification) influencing model/data misfit come into play. The assimilation of baroclinic velocity data to estimate a radiation condition for the 3-D velocity fields along the boundary, or alternatively corrections in the stratification, is left for future work. In reality, errors and uncertainties are also from a variety of other sources, including errors in the surface forcing fields, initialization, model parameterizations, as well as observations themselves. Future effort in generalizing the inverse strategy is clearly needed. In addition to continued development of dynamic model and data assimilation techniques, the importance of emergent coastal ocean observing systems cannot be overemphasized. These observing systems must have accuracy and coverage sufficient to promote improvements in the coastal ocean surface and lateral boundary condition specification via data assimilation if we are to achieve improvements in coastal ocean state variable specifications and prediction.

[42] Data assimilative hindcast reported here also reveals complex hydrodynamic structures and synoptic variability in the GOM coastal circulation, and their influences on coastal water material property transport. In particular, the complex bathymetric setting offshore of Penobscot and Casco bays can steer the currents and generate local upwelling and downwelling centers by obeying fluid con-

tinuity and kinematic boundary condition. This may have significant biological consequence and require further investigations with more in situ data in conjunction with data assimilative model simulations and diagnoses.

## References

Anderson, D. M., et al. (2005), Experimental observations and modeling of *Alexandrium fundyense* cyst dynamics in the Gulf of Maine, *Deep Sea Res., Part II*, in press.

Aretxabaleta, A., J. P. Manning, F. E. Werner, K. W. Smith, B. O. Blanton, and D. R. Lynch (2005), Data assimilative hindcast on the southern flank of Georges Bank during May 1999: Frontal circulation and implication, *Cont. Shelf Res.*, 25, 849–874.

Beardsley, R. C., D. C. Chapman, K. H. Brink, S. R. Ramp, and R. Schlitz (1985), The Nantucket Shoals Flux Experiment (NSFE79). 1. A basic description of the current and temperature variability, *J. Phys. Oceanogr.*, 6, 713–748.

Beardsley, R. C., B. Butman, W. R. Geyer, and P. Smith (1997), Physical oceanography of the Gulf of Maine: An update, in *Proceedings of the Gulf of Maine Ecosystem Dynamics Scientific Symposium and Workshop, Rep. 97-1*, pp. 39–52, Reg. Assoc. for Res. in the Gulf of Maine, Hanover, N. H.

Bennett, A. F. (1992), *Inverse Methods in Physical Oceanography*, Cambridge Univ. Press, New York.

Bigelow, H. B. (1927), Physical oceanography of the Gulf of Maine, *Bull. U.S. Bur. Fish.*, 49, 511–1027.

Bogden, P. S., P. Malanotte-Rizzoli, and R. Signell (1996), Open ocean boundary condition from interior data: Local and remote forcing of Massachusetts Bay, *J. Geophys. Res.*, 101, 6487–6500.

Bowen, A. J., D. A. Griffin, D. G. Hazen, S. A. Matheson, and K. R. Thompson (1995), Shipboard nowcasting of shelf circulation, *Cont. Shelf Res.*, 15, 115–128.

Brooks, D. A. (1985), The vernal circulation in the Gulf of Maine, *J. Geophys. Res.*, 90, 4687–4705.

Brown, W. S., and J. D. Irish (1992), The annual evolution of geostrophic flow in the Gulf of Maine: 1986–1987, *J. Phys. Oceanogr.*, 24, 2387–2412.

Ezer, T., and G. L. Mellor (1994), Continuous assimilation of Geosat altimeter data into a three-dimensional primitive equation Gulf Stream model, *J. Phys. Oceanogr.*, 24, 832–847.

Fan, Y., W. S. Brown, and Z. Yu (2005), Model simulations of the Gulf of Maine response to storm forcing, *J. Geophys. Res.*, 110, C04010, doi:10.1029/2004JC002479.

Feng, H., and W. S. Brown (1996), Wind-induced response of the western Gulf of Maine during the summer 1994, *Eos Trans. AGU*, 77(3), Ocean Sci. Meet. Suppl., OS157.

Foreman, M. G. G., R. A. Walters, R. F. Henry, C. P. Keller, and A. G. Dolling (1995), A tidal model for eastern Juan de Fuca Strait and the southern Strait of Georgia, *J. Geophys. Res.*, 100, 721–740.

Franks, P. J. S., and D. M. Anderson (1992), Alongshore transport of a toxic phytoplankton bloom in a buoyancy current: *Alexandrium tamarense* in the Gulf of Maine, *Mar. Biol.*, 112, 153–164.

Galperin, B., L. H. Kantha, S. Hassid, and A. Rosati (1998), A quasi-equilibrium turbulent energy model for geophysical flows, *J. Atmos. Sci.*, 45, 55–62.

Garfield, N., and D. L. Evans (1987), Shelf water entrainment by Gulf Stream warm-core rings, *J. Geophys. Res.*, 92, 13,003–13,012.

Geyer, W. R., R. P. Signell, D. A. Fong, J. Wang, D. M. Anderson, and B. A. Keafer (2004), The freshwater transport and dynamics of the western Maine coastal current, *Cont. Shelf Res.*, 24, 1339–1357.

Griffin, D. A., and K. R. Thompson (1996), The adjoint method of data assimilation used operationally for shelf circulation, *J. Geophys. Res.*, 101, 3457–3477.

He, R., Y. Liu, and R. H. Weisberg (2004), Coastal ocean wind fields gauged against the performance of an ocean circulation model, *Geophys. Res. Lett.*, 31, L14303, doi:10.1029/2003GL019261.

Holboke, M. J. (1998), Variability of the Maine Coastal Current under spring conditions, Ph.D. thesis, Dartmouth Coll., Hanover, N. H.

Holboke, M. J., and D. R. Lynch (1995), Simulations of the Maine Coastal Current, paper presented at 4th International Conference on Estuarine and Coastal Modeling, Am. Soc. of Civ. Eng., San Diego, Calif.

Lewis, J. K., I. Shulman, and A. F. Blumberg (1998), Assimilation of Doppler radar current data into numerical ocean models, *Cont. Shelf Res.*, *18*, 541–559.

Luettich, R. A., J. C. Muccino, and M. G. G. Foreman (2002), Considerations in the calculation of vertical velocity in three-dimensional circulation models, *J. Atmos. Oceanic Technol.*, *19*, 2063–2076.

Lynch, D. R., and C. G. Hannah (2001), Inverse model for limited-area hindcasts on the continental shelf, *J. Atmos. Oceanic Technol.*, *18*, 962–981.

Lynch, D. R., and C. E. Naimie (2002), Hindcasting the Georges Bank circulation, part II: Wind-band inversion, *Cont. Shelf Res.*, *22*, 2191–2224.

Lynch, D. R., J. T. C. Ip, C. E. Naimie, and F. E. Werner (1996), Comprehensive coastal circulation model with application to the Gulf of Maine, *Cont. Shelf Res.*, *16*, 875–906.

Lynch, D. R., M. J. Holboke, and C. E. Naimie (1997), The Maine Coastal Current: Spring climatological circulation, *Cont. Shelf Res.*, *17*, 605–634.

Lynch, D. R., C. E. Naimie, and C. G. Hannah (1998), Hindcasting the Georges Bank circulation, part I: Detiding, *Cont. Shelf Res.*, *18*, 607–639.

Lynch, D. R., et al. (2001), Real-time data assimilative modeling on Georges Bank, *Oceanography*, *14*, 65–77.

Manning, J. P., R. G. Lough, C. E. Naimie, and J. H. Churchill (2001), Modeling the effect of a slope water intrusion on advection of fish larvae: May 1995 on Georges Bank., *ICES J. Mar. Sci.*, *58*(5), 985–993.

McGillicuddy, D. J., R. P. Signell, C. A. Stock, B. A. Keafer, M. D. Keller, R. D. Hetland, and D. M. Anderson (2003), A mechanism for offshore initiation of harmful algal blooms in the coastal Gulf of Maine, *J. Phytoplankton Res.*, *25*, 1131–1138.

McGillicuddy, D. J., et al. (2005), Mechanisms regulating the large-scale seasonal fluctuations in *Alexandrium fundyense* populations in the Gulf of Maine, *Deep Sea Res., Part II*, in press.

Mellor, G. L., and T. Yamada (1982), Development of a turbulence closure model for geophysical fluid problems, *Rev. Geophys.*, *20*, 851–875.

Mellor, G. L., and T. Ezer (1991), A Gulf Stream model and an altimetry assimilation scheme, *J. Geophys. Res.*, *96*, 8779–8795.

Oke, P. R., J. S. Allen, R. N. Miller, G. D. Egbert, and P. M. Kosro (2002), Assimilation of surface velocity data into a primitive equation coastal ocean model, *J. Geophys. Res.*, *107*(C9), 3122, doi:10.1029/2000JC000511.

Pettigrew, N. R., D. W. Townsend, H. Xue, J. P. Wallinga, P. J. Brickley, and R. D. Hetland (1998), Observations of the Eastern Maine Coastal Current and its offshore extensions in 1994, *J. Geophys. Res.*, *103*, 30,623–30,639.

Pickett, M. H., W. Tang, L. K. Rosenfeld, and C. H. Wash (2003), QuikSCAT satellite comparisons with near-shore buoy wind data off the US West coast, *J. Atmos. Oceanic Technol.*, *20*, 1869–1879.

Proehl, J. A., D. R. Lynch, D. J. McGillicuddy Jr., and J. R. Ledwell (2005), Modeling turbulent dispersion on the north flank of Georges Bank using Lagrangian particle methods, *Cont. Shelf Res.*, *25*, 875–900.

Signell, R. P., H. L. Jenter, and A. F. Blumberg (1994), Modeling the seasonal circulation in Massachusetts Bay, in *Proceedings of 3rd International Conference on Estuarine and Coastal Modeling*, pp. 578–590, edited by M. L. Spaulding, Am. Soc. of Civ. Eng., Reston, Va.

Smagorinsky, J. (1963), General circulation experiments with the primitive equations I. The basic experiment, *Mon. Weather Rev.*, *91*, 99–164.

Smith, K. W. (2004), Objective Analysis for Circulation Initialization (OACI) 1.2 users' guide, Numer. Model. Lab., Dartmouth Coll., Hanover, N. H. (Available at http://www-nml.dartmouth.edu/circmods/gom.html)

Taylor, G. T. (1921), Diffusion by continuous movement, *Proc. London Math. Soc., Ser. A*, *20*, 196–221.

Townsend, D. W. (1991), Influences of oceanographic processes on the biological productivity of the gulf of Maine, *Rev. Aquat. Sci.*, *5*, 211–230.

Townsend, D. W., J. P. Christensen, D. K. Stevenson, J. J. Graham, and S. B. Chenoweth (1987), The importance of a plume of tidally-mixed water to the biological oceanography of the Gulf of Maine, *J. Mar. Res.*, *45*, 699–728.

Thompson, K. R., and D. A. Griffin (1998), A model of the circulation on the outer Scotian shelf with open boundary condition inferred by data assimilation, *J. Geophys. Res.*, *103*, 30,641–30,660.

Xue, H., F. Chai, and N. R. Pettigrew (2000), A model study of seasonal circulation in the Gulf of Maine, *J. Phys. Oceanogr.*, *30*, 1111–1135.

————————————

R. He, D. J. McGillicuddy, and C. A. Stock, Woods Hole Oceanographic Institution, Mail Stop 10, Woods Hole, MA 02543, USA. (rhe@whoi.edu)

D. R. Lynch and K. W. Smith, Thayer School of Engineering, Dartmouth College, 8000 Cummings Hall, Hanover, NH 03755-8000, USA.

J. P. Manning, Northeast Fisheries Science Center, NOAA, 166 Water Street, Woods Hole, MA 02543-1026, USA.